What can we learn from REE abundances in clinopyroxene and orthopyroxene in residual mantle peridotites?

Yan Liang[1], Zejia Ji[1,2], and Boda Liu[1,*]

1 Department of Earth, Environmental and Planetary Sciences, Brown University, Providence, RI 02912, United States

2 The Key Laboratory of Orogenic Belts and Crustal Evolution, Peking University, Beijing, 100871, China

* Now at Department of Earth, Environmental and Planetary Sciences, Rice University, Houston, TX 77005, United States

Corresponding author: Yan Liang (yan_liang@brown.edu)

Abstract

Clinopyroxene and orthopyroxene are the two major repositories of rare earth elements (REE) in spinel peridotites. Most geochemical studies of REE in mantle samples focus on clinopyroxene. Recent advances in in situ trace element analysis has made it possible to measure REE abundance in orthopyroxene. The purpose of this study is to determine what additional information one can learn about mantle processes from REE abundances in orthopyroxene coexisting with clinopyroxene in residual spinel peridotites. To address this question, we select a group of spinel peridotite xenoliths (9 samples) and a group of abyssal peridotites (12 samples) that are considered residues of mantle melting and that have major element and REE compositions in the two pyroxenes reported in the literature. We use a disequilibrium double-porosity melting model and the Markov chain Monte Carlo method to invert melting parameters from REE abundance in the bulk sample. We then use a subsolidus reequilibration model to calculate REE redistribution between cpx and opx at the extent of melting inferred from the bulk REE data and at the closure temperature of REE in the two pyroxenes. We compare the calculated results with those observed in clinopyroxene and orthopyroxene in the selected peridotitic samples. Results

from our two-step melting followed by subsolidus reequilibration modeling show that it is more reliable to deduce melting parameters from REE abundance in the bulk peridotite than in clinopyroxene. We do not recommend the use of REE in clinopyroxene alone to infer the degree of melting experienced by the mantle xenolith, as HREE in clinopyroxene in the xenolith are reset by subsolidus reequilibration. In general, LREE in orthopyroxene and HREE in clinopyroxene are more susceptible to subsolidus redistribution. The extent of redistribution depends on the modes of clinopyroxene and orthopyroxene in the sample and thermal history experienced by the peridotite. By modeling subsolidus redistribution of REE between orthopyroxene and clinopyroxene after melting, we show that it is possible to discriminate mineral mode of the starting mantle and cooling rate experienced by the peridotitic sample. We conclude that endmembers of the depleted MORB mantle and the primitive mantle are not homogeneous in mineral mode. A modally heterogeneous peridotitic starting mantle provides a simple explanation for the large variations of mineral mode observed in mantle xenoliths and abyssal peridotites. Finally, by using different starting mantle compositions in our simulations, we show that composition of the primitive mantle is more suitable for modeling REE depletion in cratonic mantle xenoliths than the composition of the depleted MORB mantle.

Introduction

Rare earth elements (REE) in mantle rocks have been widely used to study partial melting, melt migration and melt-rock interaction processes in the mantle. Most geochemical studies of REE in spinel peridotites focus on clinopyroxene (cpx) which is the major repository of REE in the peridotites. Important conclusions based on REE abundances in cpx in abyssal peridotites include (1) samples with depleted LREE are resulted from fractional or near fractional melting (Johnson et al., 1990; Johnson and Dick, 1992; Kelemen et al., 1997; Niu and Hékinian, 1997; Shimizu, 1998; Hellebrand et al., 2001; Brunelli et al., 2006; Liang and Peng, 2010); (2) samples with elevated LREE are affected by melt impregnation and melt-rock interaction (Hellebrand et al., 2002; Warren et al., 2009; Brunelli et al., 2014); and (3) cpx with higher HREE but depleted LREE is attributed to fractional melting starting in the garnet stability field (Johnson et al., 1990; Hellebrand et al., 2002; Brunelli et al., 2006). However, not all of the interpretations are unique. For example, the slightly elevated LREE patterns in abyssal peridotites that show no obvious signs

of melt addition can also be explained by small extent of disequilibrium melting (Liang and Liu, 2016; Liu and Liang, 2017). Near fractional melting starting in the garnet stability field failed to explain some samples with elevated HREE patterns (Liang and Peng, 2010). One possible explanation of the higher than expected HREE in residual cpx is subsolidus redistribution (Sun and Liang, 2014). During subsolidus reequilibration, REE is strongly and preferentially partitioning into cpx relative to orthopyroxene and olivine in spinel peridotites (e.g., Stosch, 1982; Witt-Eickschen and O'Neill, 2005; Lee et al., 2007; Liang et al., 2013; Sun and Liang, 2014). To sort out the various magmatic and subsolidus processes affecting the abundance and distribution of REE and other trace elements in residual peridotites, additional information is needed.

Recent advances in in situ trace element analysis makes it possible to measure REE and other incompatible trace elements in orthopyroxene (opx). An increasing number of geochemical studies of spinel peridotites have reported REE in both cpx and opx (e.g., Stosch, 1982; Bedini and Bodinier, 1999; Hellebrand et al., 2005; Witt-Eickschen and O'Neill, 2005; Warren et al., 2009; Brunelli and Seyler, 2010; Seyler et al., 2011; Liu et al., 2012; D'Errico et al., 2016; Quinn et al., 2018). These additional data not only can be used to reconstruct bulk trace element compositions for samples that experienced secondary alteration, but also offer an opportunity for a more complete assessment of the thermal and magmatic history experienced by the peridotite. To learn more from REE abundances in coexisting cpx and opx in residual peridotite samples, we use a disequilibrium double-porosity melting model and a subsolidus reequilibration model to investigate how REE in the bulk residue are fractionated during decompression melting along a mantle adiabat and how REE in residual cpx and opx are redistributed during subsolidus reequilibration after melting. In a closed system, REE abundance in the bulk sample is independent of subsolidus reequilibration, whereas REE abundances in coexisting cpx and opx are sensitive to temperature and mineral mode. Hence it is more advantageous to infer melting parameters from REE abundance in the bulk sample than in cpx alone.

The chief objectives of this study are twofold: (1) to develop a general method for interpreting REE in residual cpx, opx, and the bulk peridotite; and (2) to determine what more we can learn from REE concentrations in opx in addition to cpx in residual mantle peridotites. We use a general double-porosity model for disequilibrium melting in an upwelling melting column to address objective (1). In the absence of chemical disequilibrium, concentrations of REE in opx are

related to those in cpx by mineral-melt or mineral-mineral partition coefficients. Hence REE in residual cpx alone are sufficient for studying the melting history experienced by residual peridotites. This was first demonstrated in the pioneering work of Johnson et al. (1990). However, detailed modeling of REE in residual cpx in abyssal peridotites suggests that their LREE patterns can be better explained if a small extent of chemical disequilibrium is present between cpx and coexisting melt during partial melting (Liang and Liu, 2016; Liu and Liang, 2017). The present study is built on these recent modeling work by considering REE in opx in addition to cpx during disequilibrium melting. To achieve objective (2), we conduct two case studies of REE in selected residual spinel peridotites from subcontinental lithosphere (mantle xenoliths) and mid-ocean ridges (abyssal peridotites). We use the disequilibrium melting model to calculate REE concentrations in residual cpx, opx, and the bulk peridotite. We then redistribute REE between cpx and opx at their closure temperature using temperature-dependent REE opx-cpx partition coefficients and modal abundances of cpx and opx in the sample. We show that this two-step melting followed by subsolidus reequilibration modeling, which has not been done before, allows us to better match the observed REE patterns of cpx and opx in the two sets of peridotite samples. By including REE in opx in our modeling, we can learn not only the melting process but also thermal history experienced by the residual peridotites after melting. The latter is sensitive to mineral modes in the starting mantle. As will be demonstrated in this study, it is possible to constrain mineral mode in the starting mantle and thermal history of the residual peridotites based on REE abundances in both cpx and opx.

Melting followed by subsolidus reequilibration

Model description

We are interested in the fractionation of REE in bulk peridotite during decompression melting in a mantle column and the redistribution of REE between cpx and opx in the peridotite at a subsolidus temperature after melting. We use the disequilibrium double-porosity melting model of Liang and Liu (2016) to simulate REE depletion during decompression melting along a mantle adiabat. For the convenience of a reader, the governing equations are summarized in Appendix A. Key features of the disequilibrium melting model include channelized melt extraction and

diffusion-limited chemical exchange between the pyroxenes and the interstitial melt. Because diffusivities of REE in olivine and garnet are considerably larger than those in the pyroxenes (Van Orman et al., 2001, 2002; Cherniak and Liang, 2007; Cherniak, 2015) and abundances of REE in olivine and spinel are much smaller than those in the pyroxenes, it is reasonable to assume that olivine and spinel (also garnet for melting in the garnet stability field) are in local chemical equilibrium with their interstitial melt during decompression melting.

There are four dimensionless parameters in the disequilibrium double-porosity melting model for this problem: degree of melting experienced by the residual mantle (F), fraction of melt extracted to the channel ($\mathbb{R}$, called melt suction rate hereafter), disequilibrium parameter of La in cpx (ε_{cpx}^{La}), and relative diffusion rate of REE in cpx and opx grains. The melt suction rate is an important parameter of the double-porosity melting model (Iwamori, 1994; Lundstrom, 2000; Jull et al., 2002; Liang and Peng, 2010). The double-porosity model recovers the perfect fractional melting model when $\mathbb{R} = 1$ and the batch melting model when $\mathbb{R} = 0$. We refer the style of melting as near fractional when more than 75% of melt produced by peridotite melting are extracted to the channel (i.e., $0.75 < \mathbb{R} < 1$). The diffusive exchange rate constants for an REE in opx (R_{opx}) and cpx (R_{cpx}) are inversely proportional to the diffusive time scales for opx and cpx (Navon and Stolper, 1987; Bodinier et al., 1990; Liang, 2003):

$$R_{opx} = \frac{3\beta D_{opx}}{d_{opx}^2}\ ,\ R_{cpx} = \frac{3\beta D_{cpx}}{d_{cpx}^2}\ , \qquad (1a, 1b)$$

where D is the diffusion coefficient of REE in opx or cpx; d is the average or effective mineral grain size of opx or cpx; and β is a geometric factor. The relative diffusion rate for an REE is given by the expression:

$$\frac{R_{opx}^{REE}}{R_{cpx}^{REE}} = \frac{D_{opx}^{REE}}{D_{cpx}^{REE}} \frac{d_{cpx}^2}{d_{opx}^2}. \qquad (2)$$

The disequilibrium parameter is a measure of bulk melting rate relative to diffusion rate for the element of interest in a mineral (Eq. A1d in Appendix A). Given the disequilibrium parameter of La in cpx, disequilibrium parameters for other REE in cpx can be calculated according to their diffusivity ratio (Liang and Liu, 2016):

$$\varepsilon_{cpx}^{REE} = \frac{D_{cpx}^{La}}{D_{cpx}^{REE}} \varepsilon_{cpx}^{La}. \quad (3)$$

During decompression melting along a mantle adiabat, temperature decreases upward in the melting column. In this study, we calculate the relative diffusion rate and disequilibrium parameters using experimentally determined diffusion parameters for REE in cpx and opx (Van Orman et al., 2001, 2002; Cherniak and Liang, 2007). For convenience of numerical calculations, we scale the disequilibrium parameters in Eq. 3 by their respective values at 1300°C,

$$\varepsilon_{cpx}^{T} = \frac{D_{cpx}^{1300}}{D_{cpx}^{T}} \varepsilon_{cpx}^{1300} \quad . \quad (4)$$

In the simulations presented below, we treat ε_{cpx}^{1300} for La in cpx as a free parameter and calculate the disequilibrium parameter at other temperatures using Eq. 4. Variations of the disequilibrium parameter of La in cpx as a function of temperature and degree of melting along a 1300 °C mantle adiabat can be found in supplementary Fig. S1. Equilibrium melting is realized when $\varepsilon_{cpx}^{La} = 0$.

We use the temperature and major element composition dependent opx-cpx and olivine-cpx REE partitioning models of Sun and Liang (2014) and mineral mode in the sample to calculate REE abundances in coexisting opx and cpx at a subsolidus temperature after melting. In a closed system, concentration of a trace element in the bulk peridotite (C_s) depends on mineral mode and mineral composition, but is independent of temperature, viz.,

$$C_s = w_{cpx} C_{cpx} + w_{opx} C_{opx} + w_{ol} C_{ol} + w_{sp} C_{sp} , \quad (5)$$

where w_j and C_j are the weight fraction of and trace element concentration in mineral j in the residual peridotite, respectively. Since REE abundances in olivine and spinel are much lower than those in cpx and opx, concentrations of an REE in cpx and opx at a given temperature (T) can be calculated using the expressions (see also Eq. A2e in Appendix A):

$$C_{cpx}(T) = \frac{C_s}{w_{cpx} + w_{opx} k_{opx-cpx}} , \quad (6a)$$

$$C_{opx}(T) = k_{opx-cpx} C_{cpx} , \quad (6b)$$

where $k_{opx\text{-}cpx}$ is the temperature and major element composition dependent opx-cpx REE partition coefficient. In the case studies presented below, we set the temperature in Eqs. 6a and 6b to the closure temperature of REE based on the REE-in-two-pyroxene thermometer of Liang et al. (2013). According to Eqs. 6a and 6b, concentrations of REE in cpx and opx in a residual peridotite vary as a function of mineral mode and temperature even when concentrations of REE in the bulk rock are constant. The sensitivity of REE redistribution to mineral mode and subsolidus temperature will be demonstrated below.

Forward simulations of REE in pyroxenes during melting and subsolidus reequilibration

Variations of REE in opx and cpx in residual peridotites that have experienced decompression melting and subsolidus reequilibration can be visualized through forward simulations using the two-step melting followed by subsolidus reequilibration model outlined in the preceding section. Figure 1a shows one such example for a case of 6% near fractional melting ($\mathbb{R}$ = 0.95, ε_{La}^{1300} = 0.01) of spinel lherzolite along the 1300 °C adiabat. Melting strongly depletes LREE in both cpx and opx, hence the bulk rock (solid lines in Fig. 1a). Since REE abundances in cpx are considerably higher than those in opx, olivine and spinel, REE pattern of the bulk residue follows that of cpx, forming subparallel trends in the chondrite-normalized REE diagram (Fig. 1a). To the first order, REE abundance in the bulk rock is proportional to the amount of cpx in the residue, viz., $C_s \sim w_{cpx}*C_{cpx}$. This is demonstrated in Fig. 1a where the abundance of REE in cpx is about 7 times that in the bulk rock and the modal abundance of cpx in the residue after 6% melting is 13.6%. The close similarity between REE in the bulk rock and its constituent cpx forms the basis for using REE in cpx to study mantle melting processes in the literature.

Figure 1a also shows that REE pattern of residual opx differs considerable from those of cpx and the residue: light and middle REE are preferentially depleted in opx relative to those in the bulk or cpx whereas heavy REE in opx are comparable to those in the bulk rock. This is due to the smaller M2 site of opx structure, making LREE more incompatible in opx than in cpx. The net effect is a steeper LREE depleted pattern for opx in the REE diagram. The REE pattern in opx can be further complicated by subsolidus reequilibration: with decreasing temperature, LREE is preferentially redistributed from opx to cpx, shifting the entire opx REE pattern below that produced by partial melting (cf. dashed and solid green lines in Fig. 1a). Although it is not

straightforward to infer mantle melting processes based on REE abundances and patterns in opx in residual peridotites that are reset by subsolidus reequilibration, abundances of REE in opx may offer useful information on the thermal history experienced by the peridotite and mineral modes in the starting mantle, as we will demonstration through two case studies below. However, due to the ionic size-dependent REE opx-cpx partitioning, subsolidus reequilibration mildly elevates HREE in cpx (Figs. 1a and 1b), which may complicate the interpretation of garnet signal in residual spinel lherzolite and harzburgite (Sun and Liang, 2014). Since the abundance of LREE is considerably lower in residual opx, LREE in cpx are not sensitive to subsolidus redistribution in spinel lherzolite. When the degree of melting is large, the modal abundance of cpx decreases in the residue, and the effect of subsolidius reequilibration on the REE in cpx will be more significant. This is illustrated in Fig. 1b for a case of 15% near fractional melting ($\mathbb{R}$ = 0.95, ε_{La}^{1300} = 0.01).

The mineral grain size also affects REE abundances in cpx and opx during disequilibrium melting and subsequent cooling through the relative diffusive exchange rate (Eq. 2). In general, grain size of opx (2-5 mm) is larger than grain size of cpx (< 2 mm) in residual spinel peridotites. The effect of chemical disequilibrium increases with increasing opx grain size, leading to an increase in the effective or apparent partition coefficient for REE between opx and its coexisting melt (Liang and Liu, 2016). This can be demonstrated through a forward simulation in which we increase the relative opx-to-cpx grain size from 1 to 5 while keeping the cpx grain size to 1 mm. As shown in Fig. 1c, the calculated middle and heavy REE abundances in cpx slightly decrease whereas the light REE abundances in opx significantly increase compared to the case of 1 mm opx. Consequently, the simulated bulk REE is not very sensitive to the choice of opx/cpx grain size ratio. Regardless of how REE are distributed between opx and cpx, the REE abundance in the bulk residue remains the same as that produced by partial melting. Hence it is more reliable to use REE in the bulk rock to infer melting processes experienced by residual peridotites than REE in cpx alone. We will demonstrate this point through two case studies below.

Reading magmatic and thermal history from REE abundances in bulk peridotites and two pyroxenes

Strategy and methods

We use the melting followed by subsolidus reequilibration model and REE abundances in selected bulk samples and their constituent cpx and opx to infer melting and cooling processes experienced by residual peridotites. Based on forward simulations such as the ones shown in Fig. 1, we treat this problem in two sequential steps: melting and subsolidus redistribution. For the melting part, we use Bayesian analysis and the disequilibrium double-porosity melting model to invert key melting parameters (F, $\mathbb{R}$, and ε_{cpx}^{La}) from the observed REE concentrations in the bulk residual peridotite. To account for temperature-dependent diffusive exchange of REE in cpx and opx (Eq. 1), we carry out disequilibrium melting calculations along a mantle adiabat in the Bayesian analysis. Since our inversion is based on bulk REE in the peridotite, REE concentrations in cpx and opx derived from our best-fit model are not required to match the observed REE patterns in cpx and opx in the peridotite sample, as the latter concentrations can be reset by subsolidus reequilibration. For the subsolidus part of our modeling, we use Eqs. 6a and 6b and the model-predicted bulk REE concentration from the first step to calculate REE concentrations in cpx and opx at the closure temperature of REE in the two pyroxenes. The closure temperature is calculated using measured REE and major element compositions of cpx and opx in the peridotite sample and the REE-in-two-pyroxene thermometer of Liang et al. (2013). As will be shown in the two case studies below, inversion of bulk REE in residual peridotites is not sensitive to mineral modes in the starting mantle, whereas subsolidus redistribution of REE between cpx and opx is sensitive to mineral mode. Given the large variations of mineral modes in mantle peridotites (e.g., Bodinier and Godard, 2014; Warren, 2016) and uncertainties in estimating mineral modes of peridotite samples, we carry out the melting and subsolidus simulations using three choices of starting mantle mode, as detailed below. Our preferred model produces the closest match to the observed REE concentrations in the bulk rock and the two pyroxenes.

To demonstrate the advantages of the method outlined in the preceding paragraph, we model REE + Y abundances in selected spinel peridotite samples from subcontinental lithosphere (mantle xenoliths, 9 samples) and mid-ocean ridges (abyssal peridotites, 12 samples). We include Y in our analysis because it behaves similarly to HREE during mantle melting and its abundance is routinely reported along with REE in opx and cpx. Peridotites from stable cratons are generally well-equilibrated and have similar and relatively low equilibrium or closure temperatures for both major elements and REE in coexisting cpx and opx, whereas abyssal peridotites have higher

closure temperatures for REE than major elements in pyroxenes (Liang et al., 2013; Dygert and Liang, 2015; Wang et al., 2015). This is illustrated in Fig. 2 for the selected samples in this study. Since abyssal peridotites are variously serpentinized and some mantle xenoliths contain glass veins, we use measured REE + Y abundances in minerals (cpx, opx, and olivine when available) and mineral modes reported in the literature to reconstruct bulk REE + Y abundances in the peridotites. As shown in Fig. 1, the light and middle REE in opx are considerably lower than those in cpx, making accurate measurements of these elements in opx an analytical challenge. This problem is especially prevalent for odd atomic number elements such as La (57) and Pr (59), resulting in scattered LREE patterns in some samples. To include more elements and more samples in this study, we applied an interpolation/extrapolation procedure to some of the samples that exhibit scattered REE patterns. The procedure, detailed in Supplementary Materials (*REE interpolation procedure and results*), is based on correlation between the nearest neighbor REE (e.g., La and Ce) established by mantle pyroxenes that have smooth REE patterns. In Supplementary Table S1a, we list mineral modes and REE concentrations in cpx, opx, and the bulk peridotite included in this study.

In order to use the disequilibrium melting model to calculate the melting parameters from the bulk REE + Y abundances in residual peridotites, we need to know mineral grain size, mineral mode, and composition of the starting mantle. Following standard practice in REE modeling, we assume that abundances of REE + Y in the starting mantle are the same as the average depleted MORB mantle (DMM, Workman and Hart, 2005) for abyssal peridotites and the primitive mantle (PM, McDonough and Sun, 1995) for mantle xenoliths in our first round of simulations. To assess uncertainties and misfits, we also explore other starting mantle compositions. The mineralogy of the starting mantle is a primitive spinel lherzolite. (We will discuss garnet field melting in a later section.) There are some uncertainties in the mineral mode of the starting mantle. For example, the DMM of Workman and Hart (2005) consists of 13% cpx, 28% opx, 57% olivine, and 2% spinel, whereas the starting mantle of Johnson (1998) and Hellebrand et al. (2002) has 17% cpx, 27% opx, 53% olivine, and 3% spinel. The latter has been used in our inverse modeling of REE depletion in residual cpx from abyssal peridotites (Liang and Peng, 2010; Liang and Liu, 2016; Liu and Liang, 2017). Figs. 3a and 3b show large variations in mineral modes in both mantle xenoliths and abyssal peridotites. (For more peridotite data, a reader is referred to Fig. 1 in Bodinier and Godard (2014) and Fig. 4 in Warren (2016).) Even for the small number of samples included in the present study,

the range of modal variations cannot be explained by a single melting trend or melting reaction using either aforementioned starting mode. It is possible that mineral modes are not well constrained for some of the peridotite samples (e.g., heavily serpentinized abyssal peridotites, point counting of small area). It is also likely that mineral mode in the starting mantle is not uniform, considering the efficiency of mantle convection, lithological heterogeneities in the mantle, and diversity of peridotites in the field. In this study, we consider three mineral modes for the starting mantle source. To reduce the number of free parameters in our modeling, we fix the modal abundance of olivine in the mantle source to 56% or 60.5% and vary the cpx:opx proportion in the mantle source for the mantle xenolith or abyssal peridotite samples (Figs. 3a and 3b). This is a reasonable approach as (1) the relative REE pattern in the bulk rock is not very sensitive to the abundance of olivine in the mantle source, and (2) the resultant residual modes cover a wide range of mineral modal abundances (Fig. 3). Finally, the grain size of the starting mantle is unknown, although in general grain size of opx is larger than grain size of cpx in peridotites. As a starting model, we assume that the grain size ratio between opx and cpx ($\frac{d_{cpx}}{d_{opx}}$) does not change during melting. The latter helps to simplify the evaluation of the relative diffusion rate between opx and cpx (Eq. 2).

Mantle melting is non-modal. In standard geochemical treatment of non-modal melting, one uses melting reaction derived from peridotite melting studies. The coefficients of the melting reaction are constant and residual mineral modes vary linearly as a function of F in the melting column. In this study, we use the melting reaction of Baker and Stolper (1994) for spinel lherzolite in our inverse modeling of REE + Y in the bulk mantle xenoliths. This standard geochemical approach is adequate for modeling REE in mantle xenoliths as detailed melting processes experienced by the lithospheric mantle are not well understood. To model garnet-field melting in a self-consistent way for abyssal peridotites, we use mineral modes derived from pMELTS (Ghiorso et al., 2002) simulation of decompression melting along an adiabat. In this pMELTS based model, mineral modes (w_j in Eqs. A2a-A2e in Appendix A) vary somewhat nonlinearly as a function of F in the melting column (the three curves in Fig. 3b). Nonetheless, the average melting reaction derived from the pMELTS based modeling is very similar to the 1 GPa melting reactions of Baker and Stolper (1994) and Kinzler and Grove (1992) for spinel lherzolite (see Table 2 in Walter, 2014). As detailed in the section *Case study 2: Abyssal peridotites*, this

pMELTS based modeling allows us to eliminate a free parameter in garnet-field melting. With the stated choices of mineral modes and melting reactions, our melting model is able to cover most of the observed variations in mineral modes in the selected mantle samples (Figs. 3a and 3b).

The disequilibrium double-porosity melting model summarized in Appendix A consists of three coupled nonlinear ordinary differential equations and one algebraic equation for spatial variations of a trace element in interstitial melt, cpx, opx, and bulk residue (Eqs. A2a-A2d). They have no analytical solutions for the problem outlined above. Hence, we cannot use nonlinear least squares analysis to invert melting parameters as we did for REE in cpx (Liang and Peng, 2010; Liang and Liu, 2016). To get around this difficulty, we use Markov chain Monte Carlo (MCMC) method to invert the melting parameters F, ε_{cpx}^{1300}, and $\mathbb{R}$ from REE + Y concentrations in the bulk sample. MCMC methods are a class of powerful statistical tools for solving nonlinear inverse problems in Bayesian analysis (e.g., Sambridge and Mosegaard, 2002). Liu and Liang (2017) used MCMC to invert melting parameters from REE abundance in residual cpx in abyssal peridotites. The present work follows the inversion procedure detailed in their study. To facilitate MCMC inversion, we set bounds for the disequilibrium parameter ε_{cpx}^{1300} to [0, 0.15] and the melt suction rate $\mathbb{R}$ to [0, 1], based on previous inversion results using similar model or method (Lundstrom, 2000; Liang and Peng, 2010; Liang and Liu, 2016; Liu and Liang, 2017). We run 10,000 to 50,000 simulations for each sample to ensure convergence and use the result to calculate best fitting parameters and uncertainties. The best fitting parameters are then used to calculate REE abundances in the bulk sample, residual cpx and opx, and chemically re-equilibrated cpx and opx at closure temperatures in the two pyroxenes. Below we present results from two case studies.

Case study 1: Mantle xenoliths

To demonstrate the basic feature of the disequilibrium melting model and the effect of subsolidius redistribution, we select 9 well-characterized spinel lherzolite and harzburgite xenoliths from the literature: 3 samples from Yangyuan, North China Craton (Liu et al., 2012), 1 sample from West Eifel, Germany (Witt-Eickschen and O'Neill, 2005), 1 sample from East Africa Rift (Bedini and Bodinier, 1999), 3 samples from Kilbourne Hole, New Mexico (Harvey et al., 2012), and 1 sample from the Coast Ranges of central California (Quinn et al., 2018). These

samples are protogranular, free of garnet, plagioclase, hydrous minerals, and veins. They are selected on the basis of their depleted light REE patterns in cpx and opx, well-defined linear trends for at least the middle and heavy REE in the inversion diagram of the REE-in-two-pyroxene thermometer, and similar equilibrium temperatures between major element-based and REE-based pyroxene thermometers. Figure 2 shows that the calculated temperatures are generally below the solidus of the peridotite xenoliths. Figure 3a displays modal abundances of the selected samples. For reference, we plot selected major element concentrations in these samples as a function of bulk MgO content and spinel Cr# (= 100Cr/Cr+Al, in molar) in supplementary Figs. S2a and S2b. Supplementary Tables S1b and S2 and Fig. S4 present results of MCMC simulations with PM and DMM starting compositions for the nine xenolith samples along the 1300°C mantle adiabat (Fig. S1). Figure 4 shows an example of MCMC simulations for sample CK-2 from the Coast Ranges of central California (Quinn et al., 2018). Figure 5 presents the best fit models for the nine xenoliths with PM starting compositions. The main results are summarized below.

First, the bulk REE patterns are well reproduced by the disequilibrium double-porosity melting model. The quality of fit is not very sensitive to the choice of starting mantle mode (cf. Figs. 4a-4c). This is shown by the similar Pearson's Chi-squares among the three cases for each sample (Supplementary Table S2). Here we calculate Pearson's Chi-square for the bulk REE after inversion using the expression:

$$\chi^2_{bulk} = \sum_{j=1}^{N} \frac{\left(C_{s,j} - C^m_{s,j}\right)^2}{C_{s,j}}, \quad (7)$$

where $C_{s,j}$ and $C^m_{s,j}$ are the model-derived and measured bulk solid concentrations for element j, respectively; N (= 14) is the number of elements in the model. In general, the smaller the Pearson's Chi-square, the better the model prediction will be. There is a small trade-off between cpx abundance in the starting mantle and the degree of melting: the higher the cpx mode in the starting mantle, the greater the degree of melting is required to match the observed depletion in REE in the bulk residue. Increasing cpx mode from 14% to 20% in the starting mantle results in 0.11~3% increase in the inferred degree of melting for the nine xenolith samples.

Second, the observed REE patterns in residual cpx and opx (filled blue and green circles in Figs. 4 and 5) cannot be reproduced directly using melting parameters derived from the bulk

373 REE pattern (blue and green solid lines). Very often, LREE in opx is overestimated and HREE in
374 cpx is underestimated by the melting model, which appears to be consistent with the subsolidus
375 reequilibration trends displayed in Fig. 1. To quantify the effect of subsolidius redistribution, we
376 recalculated the model-derived REE concentrations in opx and cpx using the temperature and
377 major element composition dependent REE opx-cpx partition coefficients (Sun and Liang, 2014)
378 and closure temperatures (T_{REE}) derived from the REE-in-two-pyroxene thermometer (Liang et al.,
379 2013). The latter is 964°C for sample CK-2. (T_{REE} for the nine xenoliths are provided in Fig. 5.)
380 Figures 4 and 5 (see also supplementary Fig. S4) show that the matches to the measured REE
381 patterns in cpx and opx in the nine xenolith samples are considerably improved after adjustment
382 of subsolidus redistribution. This is an important new result from this study.

383 Finally, for a given sample, our preferred starting mantle mode and melting parameter
384 should have the smallest sum of Pearson's Chi-squares for the bulk peridotite, cpx, and opx among
385 the three starting mantle modes, where Pearson's Chi-squares for cpx and opx are calculated after
386 adjustment for subsolidus reequilibration. Figure 5 summaries results of our preferred model and
387 Supplementary Table S2 provides additional information on uncertainties of our preferred melting
388 parameters and Pearson's Chi-squares. To facilitate discussion, we also invert melting parameters
389 from REE in cpx alone using the disequilibrium melting model of Liu and Liang (2017). It is
390 interesting to note that the quality of fit to REE patterns in cpx is comparable to that based on
391 inversion of REE in cpx alone, as the calculated Pearson's Chi-squares for cpx from the bulk model
392 and cpx alone model are very similar for the nine samples (Supplementary Table S2). The misfits,
393 if present, are mostly LREE in opx and cpx. (We will discuss the misfits in a later section.) Figure
394 4 and supplementary Fig. S4 also show that the recalculated REE patterns in model-derived opx
395 and cpx (dashed lines) are sensitive to starting mantle mode. This is highlighted by the large
396 differences in the sum of Pearson's Chi-squares among the three choices of mantle mode (e.g.,
397 0.94, 4.25, and 15.2 for 14%, 17%, and 20% cpx in the starting mantle, respectively for sample
398 CK-2). Hence by modeling REE redistribution among cpx, opx, and olivine in the mantle xenolith
399 after melting, it is possible to constrain mineral mode of the starting mantle. Preferred mineral
400 modes in the starting mantle for the nine xenoliths are listed in Fig. 5.

401

402 **Case study 2: Abyssal peridotites**

Trace element abundances in cpx in abyssal peridotites have been widely used to study melting and melt-rock interaction processes beneath mid-ocean ridges (e.g., Johnson et al., 1990; Kelemen et al., 1997; Hellebrand et al., 2002, 2005; Salters and Dick, 2002; Hellebrand and Snow, 2003; Brunelli et al., 2006; Warren et al., 2009; Brunelli and Seyler, 2010; D'Errico et al., 2016). Detailed modeling of REE patterns in residual cpx in abyssal peridotites from Central Indian Ridge (data from Hellebrand et al., 2002) using an equilibrium double-porosity melting model revealed a systematic difference between measured and calculated HREE in cpx: model predicted HREE in cpx are often slightly lower than those measured in actual samples (see Fig. 8 in Liang and Peng, 2010). To fit the HREE in cpx, one can decrease the extent of melting, but this would result in an over estimation of LREE in cpx. One way to get around this dilemma is by allowing small extent of chemical disequilibrium for LREE in cpx (Liang and Liu, 2016; Liu and Liang, 2017), which hinders the depletion of LREE in cpx. This is consistent with diffusion of REE in diopside (Van Orman et al., 2002). Another possible way to elevate HREE in cpx is through subsolidus reequilibration, as we demonstrated in previous sections. However, the extent of subsolidus redistribution may be limited due to higher REE closure temperatures recorded in abyssal peridotites (Fig. 2). Yet another mechanism to produce depleted LREE and elevated HREE in cpx is to start melting in the garnet stability field (e.g., Johnson et al., 1990; Hellebrand et al., 2002; Brunelli et al., 2006).

To critically assess the roles of garnet field melting, finite rate of chemical exchange for LREE, and subsolidus redistribution of REE between cpx and opx in affecting REE patterns in abyssal peridotites, we select 12 residual abyssal peridotites from the literature that reported REE abundances in both cpx and opx: 4 samples from eastern Southwest Indian Ridge (SWIR, Seyler et al., 2011), 2 samples from Gakkel Ridge (D'Errico et al., 2016), 4 samples from western SWIR (Warren et al., 2009), and 2 samples from Central Atlantic Ridge (Brunelli and Seyler, 2010). Based on the criteria of Warren (2016), these samples are residual peridotites as they are free of plagioclase and melt veins, have low TiO_2 in spinel and depleted LREE patterns in cpx and opx. Similar to mantle xenoliths, these samples also have well-defined linear trends for at least the middle and heavy REE in the inversion diagram of the REE-in-two-pyroxene thermometer. Fig. 3b display modal abundances of the selected samples. For reference, we also plot major element compositions of the samples as a function of bulk MgO content and spinel Cr# in supplementary Figs. S3a and S3b.

Previous experimental studies have demonstrated that melting reaction of peridotite varies systematically with pressure (e.g., Kinzler and Grove, 1992; Baker and Stolper, 1994; Walter and Presnall, 1994). The extent of melting in the garnet stability field is a free parameter in most geochemical studies of REE fractionation during garnet peridotite melting, with values ranging from less than 1% to more than 10% (e.g., Johnson et al., 1990; Hellebrand et al., 2002; Brunelli et al., 2006; Liang and Peng, 2010). This free parameter can be eliminated by considering the thermodynamics of peridotite melting. In this study, we use pMELTS (Ghiorso et al., 2002) to calculate mineral mode along an adiabatic melting path that has a potential temperature of 1330℃. The starting mantle (DMM) contains 150 ppm water and melting starts in the garnet stability field. In this pMELTS-based model, the maximum extent of melting in the garnet stability field is 0.7% and the cpx exhausts at $F = 20\%$. There is no clear experimental nor geophysical evidence for the presence of high-porosity channels at depth greater than 60 km beneath mid-ocean ridges. Based on 2D double-porosity ridge modeling of Liu and Liang (2019), high-porosity channels initiating at depth less than 60 km can better explain geophysically inferred high-porosity region beneath the ridge axis (Yang et al., 2007; Key et al., 2013). In the absence of high-porosity channels, the melting suction rate reduces to zero in the double-porosity model (i.e., $\mathbb{R} = 0$). For this reason, we use batch melting to model decompression melting in the garnet stability field for abyssal peridotites. Figure 3b displays variations of mineral mode in residual peridotites calculated using pMELTS for three choices of starting mantle mineralogy (solid curves). These residual trends bracket the observed modal variations in the selected samples. Figure 6 shows an example of MCMC simulations for sample Van 7-85-49 from Western SWIR (Warren et al., 2009). Figure 7 summaries results of our preferred model for the 12 abyssal peridotite samples. Supplementary Fig. S5 presents detailed simulation results for individual samples. Supplementary Tables S1c and S2 provide additional information on uncertainties of our preferred melting parameters, Pearson's Chi-squares, and results from cpx alone inversion. The main results are summarized below.

Similar to the case of mantle xenolith, the disequilibrium double-porosity melting model can fit the bulk REE patterns very well for most of the abyssal peridotite samples included in this study (Fig. 7). The exceptions are sample Van7-96-38 from Western SWIR (Warren et al., 2009) and sample Dr 23-3-2 from Eastern SWIR (Seyler et al., 2011) which exhibit some misfits in light and middle REE (Fig. 7 and Fig. S5). (We will discuss the misfits in the next section.) As in the case of mantle xenolith, the quality of fit to the bulk REE data is not very sensitive to the starting

mantle mode, and the match to the measured REE in cpx and opx depends strongly on the starting mantle mode (cf. the three cases in Fig. 6, for other samples see Fig. S5). Overall, the matches to the observed REE patterns in cpx and opx are improved after adjustment of subsolidus redistribution (cf. solid and dashed lines in Fig. 7). However, the improvement is moderate because of the relatively high T_{REE} for the peridotite samples and very small adjustment for REE in cpx. This may result from incomplete reequilibration of REE between cpx and opx, as we discuss below. Supplementary Table 2 lists melting parameters of our preferred model for the 12 abyssal peridotite samples based on the sum of Pearson's Chi-squares of the bulk and subsolidus redistributed cpx and opx.

Discussion

Misfits of REE in the bulk samples

Although the disequilibrium double-porosity melting model can account for most of the variations of REE + Y in the bulk peridotites, noticeable misfits in the light and middle REE are observed in samples Van7-96-38 (from Western SWIR, Warren et al., 2009) and Dr23-3-2 (from eastern SWIR, Seyler et al., 2011, see Figs. 7 and S5). In both cases, the model-predicted La, Er, Tm and Yb in the bulk residue are higher than, whereas the predicted Nd, Sm, E, Gd and Tb are lower than, measured values in the samples. This humped feature is not sensitive to starting mantle mode, and is also present in the cpx-alone inversion models. Addition of melt would elevate La in cpx and opx and hence cannot explain the depleted LREE patterns in the two samples. The lower than expected bulk La, Er, Tm and Yb can be accounted for by increasing the degree of melting, but this would result in additional misfits in Nd, Sm, E, Gd and Tb. Since partition coefficients of middle REE in cpx are higher than those in garnet and the partition coefficients of HREE in cpx are lower than those in garnet, prolonged melting in the garnet stability field can produce the humped middle REE pattern in cpx and the bulk residue (e.g., Johnson et al., 1990). Our pMELTS based model for abyssal peridotites includes 0.7% initial melting in the garnet field. To further explore the role of garnet field melting, we consider a hypothetic case in which batch melting in the garnet stability field is 4.1%. Supplementary Fig. S6 presents the simulation results. The simulated bulk rock and pyroxene REE patterns after 4.1% batch melting in the garnet field show

only a small improvement for sample Dr23-3-2 (the sum of Pearson's Chi-squares decreases from 3.8 to 3.3 which is still higher than the other 10 abyssal peridotites) and no improvement at all for sample Van7-96-38. Hence the misfits are unlikely due to batch melting in the garnet stability field. Although fractional melting of garnet lherzolite can produce humped REE in cpx (Johnson et al., 1990), the physical mechanism for fractional melting in the garnet stability field remains uncertain.

Abyssal peridotites are heavily altered by serpentinization. It is possible that mineral modes in these two samples are not accurately determined. To explore this possibility, we reconstruct two new modal abundances for the two samples: one by increasing cpx mode by 2% and decreasing opx mode by 2%, and the other by decreasing cpx mode by 2% and increasing opx mode by 2%. We run MCMC simulations followed by subsolidus redistribution for these 4 cases and the results are shown in supplementary Fig. S7. Changing cpx mode by ±2% in the samples does not lead to a significant improvement in the fit to the reconstructed bulk REE in these two samples (i.e., the humped pattern persists). However, addition of 2% cpx does result in moderate improvement in the match to the observed REE patterns in cpx and opx in the two samples. This is confirmed by the smaller sum of Pearson's Chi-squares for the +2% cpx case.

We should point out that none of the hypotheses explored in this section can explain the humped REE pattern in cpx using the cpx-alone inversion model. In theory, one can match the observed REE pattern in bulk residue by judiciously adjusting starting mantle composition. It is possible that composition of the starting mantle for these two samples are different from DMM. We will come back to this point in the section **Mantle source composition**.

Misfits of LREE in opx and cpx: Incomplete reequilibration?

A common misfit shared by all the abyssal peridotite samples and four of the nine mantle xenoliths (ET80, CK-2, YY-26B, and KN03-25) in this study is that model-derived LREE (La + Ce + Pr ± Nd) are lower in cpx but higher in opx than measured values in cpx and opx, respectively. The misfit, which persists even after adjustment of subsolidus re-distribution, can be visualized by plotting the apparent opx/cpx REE partition coefficient against REE ionic radius: the apparent partition coefficients for the middle and heavy REE follow closely to an isotherm, whereas those for LREE are gradually displaced above the isotherm, defining a spoon-shaped or U-shaped pattern

(Figs. 8a and 8b). In the inversion diagram for the REE-in-two-pyroxene thermometer, the displaced LREE fall below the linear trend established by the heavy and middle REE and are excluded from the temperature calculation (Liang et al., 2013). Spoon- or U-shaped opx/cpx REE partitioning pattern is a common feature among mantle samples (e.g., Stosch, 1982; Agranier and Lee, 2007; Seyler et al., 2011). It arises when LREE in opx and cpx are out of chemical equilibrium. Agranier and Lee (2007) identified two mechanisms that can produce U-shaped disequilibrium patterns in mantle xenoliths from Dish Hill, California and abyssal peridotites from the Gakkel Ridge: diffusive fractionation at subsolidus state or metasomatism introduced by "injection and subsequent freezing in of small amounts of melt" under lithospheric or asthenospheric conditions. The 9 mantle xenoliths and 12 abyssal peridotite samples included in the present study are all depleted in LREE. Given that our disequilibrium double-porosity melting model can fit the bulk REE patterns very well in these samples, we can rule out the melt addition hypothesis for these samples.

We suggest that the spoon- or U-shaped opx/cpx REE partitioning patterns can be produced by disequilibrium melting followed by diffusive exchange between cpx and opx at subsolidus state. Figures 8a and 8b compare the apparent opx/cpx REE partition coefficients calculated from the measured REE abundances in opx and cpx in mantle xenolith CK-2 from the Coast Ranges of central California (Quinn et al., 2018, filled circles) and abyssal peridotite Van7-85-49 from western SWIR (Warren et al., 2009) with those calculated using melting parameters derived from our MCMC simulations (magenta lines). (Similar plots for other samples included in this study are presented in supplementary Figs. S4 and S5.) In both samples, the simulated apparent partition coefficients at the end of melting are displaced above the measured values. Since opx/cpx REE partition coefficients decrease with the decrease of temperature (cf. the three isotherms in Fig. 8) and diffusion coefficients of REE in cpx increase systematically from La to Lu at a given temperature (Van Orman et al., 2001, 2002; see also supplementary Fig. S1c), time scales for diffusive exchange between opx and cpx in a closed system are longer for LREE than HREE (see Fig. 5 in Liang, 2014). During diffusive reequilibration, HREE approach opx/cpx equilibrium partitioning faster than LREE. Depending on thermal history experienced by the samples (e.g., cooling and upwelling rates), the elevated opx/cpx REE patterns produced by disequilibrium melting (magenta lines in Fig. 8) would be gradually relaxed to the spoon-shaped pattern recorded in the peridotite samples (filled circles). As a proof-of-concept, we carry out two forward

simulations of diffusive reequilibration of REE between opx and cpx under two prescribed cooling rates. In this simple demonstration, cooling starts at the end of melting and terminates at the closure temperature of REE (i.e., $T = T_{REE}$). Figures 8a and 8b show that the results are promising (thin orange lines). In a more complicate but realistic situation, the cooling rate, which is likely very different for the mantle xenolith and abyssal peridotite, may vary as a function of time. Hence it may be possible to deduced cooling rate through detailed modeling of the spoon-shaped opx/cpx REE patterns in residual peridotites, a subject we will pursue in the future.

Mantle source composition

The starting mantle composition (DMM vs. PM) affects our inversion results. The depleted MORB mantle or DMM has been widely used in REE modeling of abyssal peridotites. In their original studies of mantle xenoliths, Liu et al. (2012) and Harvey et al. (2012) anchored their major and trace element data to the primitive mantle of McDonough and Sun (1995), whereas Quinn et al (2018) used HREE in their samples and DMM of Workman and Hart (2005) to infer the extent of melting. We used the primitive mantle of McDonough and Sun (1995) as the starting mantle composition in our inversion of the mantle xenolith data (Fig. 5). Composition of the mantle source is unlikely homogeneous, even for a suite of depleted samples from the same locality. Liu et al. (2012) reported Nd and Hf isotopic compositions of cpx for the three North China Craton samples (YY-26, YY-40B, and YY-42) included in this study. They found that samples YY-40B and YY-42 have considerably higher $^{143}Nd/^{144}Nd$ and $^{176}Hf/^{177}Hf$ ratios than sample YY-26 and suggested that samples such as YY-26 might be affected by melt addition via melt-rock interaction. As shown in Fig. 5, REE patterns in the bulk sample, cpx, and opx in YY-26 can be well reproduced by our two-step melting followed by subsolidus reequilibration model using PM as the starting mantle composition (see also Fig. S4). The misfit is LREE in opx, which is likely resulted from incomplete reequilibration at a low temperature (T_{REE} = 889 °C). The higher $^{143}Nd/^{144}Nd$ and $^{176}Hf/^{177}Hf$ ratios in samples YY-40B and YY-42 suggest that these samples may have derived from a more depleted mantle source. To test this hypothesis, we run MCMC simulations for samples YY-40B and YY-42 using DMM as our starting mantle composition. The results are summarized in Supplementary Table S2 and Fig. S4: the fits to sample YY-40B are slightly improved as the sum of Pearson's Chi-squares decreases from 1.76 (PM) to 1.68 (DMM), whereas no improvement is observed for

YY-42 as the sum of Pearson's Chi-squares increases from 0.62 (PM) to 1.21 (DMM). In fact, inversion of the remaining 7 xenolith samples with DMM starting composition leads to moderate to significant reduction in the quality of fits to the observed REE patterns (i.e., the sum of Pearson's Chi-squares has increased, Fig. S4). This intriguing result suggests that composition of PM is more suitable for modeling REE depletion in the nine residual mantle xenoliths included in this study. Given the slight improvement of fits to sample YY-40B using DMM starting mantle composition, we include inversion results with DMM starting composition in our discussion (two points connected by red dashed lines in Figs. 9a, 10a, 10c, and 11 below).

Composition of the average DMM is a convenient common start point in modeling REE depletion in abyssal peridotites. According to Warren et al. (2009), $^{143}Nd/^{144}Nd$ ratios in cpx in the 4 samples from SWIR (Van7-85-42, Van7-85-47, Van7-85-49, and Van7-96-38) are more similar to the depleted endmember of DMM (D-DMM) of Workman and Hart (2005) than the average DMM (see Fig. 5a in Warren et al., 2009). Intrigued, we run MCMC simulations again for the 4 samples using REE + Y in the D-DMM of Workman and Hart (2005) as the starting mantle composition. The results are presented in supplementary Fig. S8: the fits to the observed REE in the bulk, cpx, and opx are slightly improved as the sums of Pearson's Chi-squares for the 4 samples are all reduced. The small improvement is probably due to the fact that concentration differences between D-DMM and DMM of Workman and Hart (2005) are small. As noted earlier, concentrations of Pr to Eu in sample Van7-96-38 are underestimated in our models (Fig. 7). It is possible that the starting mantle for Van7-96-38 is more depleted than D-DMM. Existence of ultra-depleted mantle domains have been proposed for magma genesis beneath mid-ocean ridges based on Os, Nd, and Hf isotope ratios in residual peridotites and olivine-hosted melt inclusions (e.g., Liu et al., 2008; Stracke et al., 2011, 2019; Sanfilippo et al., 2019). The mantle source composition for residual abyssal peridotites such as the ones examined in this study is likely more variable than that represented by the DMM model of Workman and Hart (2005). More study is needed to quantify the abundances of REE and other trace elements in these extremely depleted mantle sources.

Mantle source mode

The starting mantle mode also affects fitting results. Our original purpose of exploring 3~6% variations in cpx and opx modes in the starting lherzolitic mantle was to understand the large variations in mineral modal abundance observed in the mantle xenoliths and abyssal peridotites included in this study, as such variations cannot be produced by melting a single mantle source. It turns out that the quality of fits to the bulk REE in the mantle xenoliths and abyssal peridotites are not very sensitive to the starting mantle mode, albeit a trade-off between cpx mode in the starting mantle and the inferred degree of melting. This is explained by the very similar bulk REE partition coefficients for the three starting mantle modes: they are subparallel to each other in the spider diagram (see supplementary Fig. S9). Hence one cannot use bulk REE in residual peridotite to discriminate starting mantle mode. However, REE abundances in residual cpx and opx are sensitive to starting mantle mode for the mantle xenoliths and abyssal peridotites. This is due simply to mass balance and temperature-dependent opx/cpx and ol/cpx REE partition coefficients (Eqs. 5 and 6). During subsolidus reequilibration in a closed system (i.e., for a constant C_s in Eq. 5), concentrations of REE in opx and ol in lherzolite or harzburgite decrease with the decrease of temperature, whereas concentrations of REE in cpx increase. At a given temperature, the change of concentration depends on mineral mode (cf. Figs. 2a and 2b) which, in turn, is sensitive to the starting mantle mode and the melting reaction. During subsolidus reequilibration, cpx and opx modes and major element compositions also change due to pyroxene exsolution and subsolidus reaction among the mantle minerals, which complicates the application of Eq. 6. A preliminary pMELTS-based study suggests that these major element effects are small to moderate on REE re-distribution in peridotites (Yao, 2015). Results from this study suggest that the mineral mode in the starting mantle is not homogeneous and should be taken into consideration in detailed modeling of REE and other trace elements during mantle melting. This is consistent with the scattered correlations between the bulk MgO and major and minor elements (CaO, Al_2O_3, Na_2O, and TiO_2) in the mantle xenoliths and abyssal peridotites (supplementary Figs. S2a and S3a).

Comparing extent of melting derived from REE in the bulk and REE in cpx

In general, degrees of melting based on MCMC inversion of REE + Y in the bulk samples (designated as F_{bulk} hereafter) and cpx alone (F_{cpx}) are positively correlated (Fig. 9). Figure 9a compares our estimated F_{bulk} with F_{cpx} for the nine xenoliths. Samples CK-2 (Coast Ranges of

643 central California, Quinn et al., 2018) and ET80 (East African Rift, Bedini and Bodinier, 1999)
644 are considerably more fertile in terms of spinel Cr# and contain 12.4% and 15.8% cpx, respectively.
645 Hence REE + Y in cpx in these two samples should be less affected by subsolidus redistribution.
646 Indeed, the calculated degrees of melting for CK-2 and ET80 based on the disequilibrium double-
647 porosity melting model (3.7% and 3.9%) are essentially the same as that derived from HREE in
648 cpx (2.9% and 4.2%, Supplementary Table S2). Nonetheless, light and middle REE in opx in these
649 samples are strongly affected by subsolidus redistribution, which is consistent with their low T_{REE}
650 (964℃ and 952°C, respectively). The remaining seven xenolith samples are more depleted. Except
651 sample YY-42, their inverted F_{bulk} are 2~6% higher than F_{cpx}. Sample YY-42 from North China
652 Craton (Liu et al., 2012) has the lowest cpx mode (4%, a harzburgite), the highest spinel Cr#, and
653 the second highest F_{bulk} (19%) among the nine xenolith samples included in this study. This is in
654 contrast to the rather small F_{cpx} for this sample (11%, Table S2). Given its very refractory nature,
655 we suspect that a large fraction of cpx in this sample may have derived from exsolution of opx
656 after melting. Hence the degree of melting inferred from cpx alone in this sample is not meaningful.
657 Caution should be exercised when inferring extent of melting using REE abundance in cpx in
658 harzburgitic mantle xenoliths.

659 Given the relatively high T_{REE} recorded by the 12 abyssal peridotite samples (Fig. 2) and
660 the limited extent of subsolidus redistribution of REE between cpx and opx (Fig. 7), it is not
661 surprising that the inferred degrees of melting based REE in the bulk samples are only slightly
662 higher than those derived from REE in cpx alone (Fig. 9b). The maximum difference is only 2.2%.
663 Hence in the absence of bulk REE data, one can use REE in cpx to infer the extent of melting
664 experienced by residual abyssal peridotites.

665

666 **Variations of extent of melting derived from bulk REE with key melting indices**

667 Chromian spinel has been widely used in studies of abyssal peridotites and peridotites from
668 other tectonic settings (e.g., Dick and Bullen, 1984). Hellebrand et al (2001) showed that spinel
669 Cr# in residual abyssal peridotites are strongly and inversely correlated with HREE abundances in
670 cpx in the peridotites and developed empirical equations relating degree of melting to spinel Cr#
671 for abyssal peridotites. Figure 10a shows the positive correlation between our inverted F_{bulk} and
672 spinel Cr# for the xenolith and abyssal peridotite samples included in this study. The abyssal

673 peridotites are bracketed by the batch melting and perfect fractional melting trends of Hellebrand
674 et al. (2011). However, due to the low spinel Cr#, the mantle xenolith data are mostly plotted below
675 the batch melting trend (open symbols in Fig. 10a). The latter may in part be due to subsolidus
676 redistribution of Cr and Al in spinel peridotite (e.g., Voigt and von der Handt, 2011). Caution
677 should be exercised when inferring extent of melting using Cr# of spinel in well-equilibrated
678 mantle xenoliths.

679 Our inferred degrees of melting for the mantle xenoliths and abyssal peridotites are
680 consistent with the observed variation trends of the major and minor elements in the samples. For
681 example, with increasing degree of melting, MgO in the bulk residue increases from the starting
682 DMM or PM (Fig. 10b), whereas CaO, Al_2O_3, Na_2O, and TiO_2 in the bulk sample decrease (Figs.
683 S2c and S3c). The scatteredness of the data shown in Figs. 10b, S2c and S3c can be attributed to
684 variations in mineral modes, hence major element composition, in the starting mantle.

685

686 **What have we learned from REE abundances in residual pyroxenes and peridotites?**

687 LREE depleted spinel peridotites are generally interpreted as residues of mantle melting.
688 Through case studies of carefully selected residual spinel peridotites from two distinct tectonic
689 settings we have demonstrated the advantages of using REE abundances in both the bulk rock and
690 constituent minerals (cpx and opx) in deducing magmatic and thermal history of the peridotites.
691 REE abundances in bulk residual peridotites are well-suited for studying melting process, provided
692 their concentrations are accurately determined, and grain size and mineral mode are known. As a
693 first application, we kept opx and cpx grain size ratio constant in our MCMC inversion. This is
694 likely a simplification, as we do not know how grain sizes of cpx and opx vary during mantle
695 melting and subsolidus reequilibration. LREE in opx and HREE in cpx are more susceptible to
696 subsolidus redistribution. The extent of redistribution depends on cpx and opx abundances in the
697 sample and thermal history experienced by the peridotite. We have shown that, by modeling
698 subsolidus redistribution of REE between opx and cpx after melting, it is possible to discriminate
699 mineral mode of the starting mantle. HREE in cpx in less primitive spinel lherzolite and
700 harzburgite from subcontinental lithosphere are significantly reset by subsolidus reequilibration
701 over geologic time. We do not recommend the use of REE in cpx alone to study mantle melting
702 process in such samples. The harzburgite YY-42 from North China Craton (Liu et al., 2012) is an

703 extreme example. In the absence of REE abundance in opx, REE in cpx in residual abyssal
704 peridotites can be used to infer the degree of melting of samples that experienced small to moderate
705 extent of melting. HREE in highly depleted harzburgite may be affected by subsolidus
706 reequilibration. By modeling REE abundances in the bulk and constituent cpx and opx, it is also
707 possible to discriminate starting mantle composition. Results from this study has lent support to
708 the common practice of using composition of the primitive mantle to model REE depletion in
709 cratonic mantle xenoliths and composition of DMM to model REE depletion in residual abyssal
710 peridotites. REE patterns in some of the isotopically more depleted abyssal peridotites such as the
711 four samples from SWIR (Warren et al., 2009) can be better explained by a starting mantle that is
712 more depleted than the average DMM.

713 The mantle xenoliths and residual abyssal peridotites examined in this study are a small
714 fraction of xenolith samples (9 out of 71) and abyssal peridotite samples (12 out of 60) analyzed
715 in the original studies cited in *Case study* 1 and *Case study* 2. To focus on REE depletion in the
716 bulk peridotite produced by partial melting, we exclude samples that have LREE enriched patterns,
717 samples that may have been affected by melt addition, and samples that exhibit disequilibrium
718 partitioning in HREE between opx and cpx. In spite of our conservative approach in sample
719 selection, we find that it is still not possible to reproduce REE + Y patterns in the bulk and
720 pyroxenes in these two groups of highly selective mantle peridotites using a starting mantle with
721 constant mineral mode. It is well known that the upper mantle is chemically (e.g., enriched vs.
722 depleted) and lithologically (e.g., peridotite vs. pyroxenite) heterogenous. Results from the present
723 study suggests that the endmembers of the primitive and depleted peridotitic upper mantle are also
724 modally heterogeneous. A modally heterogeneous mantle source provides a simple explanation
725 for the large variations of mineral mode observed in peridotitic mantle xenoliths and abyssal
726 peridotites. An implication of a modally heterogeneous mantle is that REE abundances of the
727 mantle source (DMM or PM) likely vary with mineral mode, i.e., a modally heterogeneous mantle
728 must also be chemically heterogeneous. A mantle source with constant and uniform composition
729 and mineral mode is merely a convenient starting point in trace element modeling of mantle
730 melting. Although adequate for examining broad variation trends of a suit of peridotitic samples,
731 a uniform mantle source is not sufficient to account for detailed variations of REE in both the bulk
732 peridotite and its constituent minerals, as demonstrated in this study.

Finally, we note that the methodology developed in this study can also be applied to other trace elements in residual peridotites, provided their diffusion in and partitioning between mantle minerals are well characterized. A potential target is the high field strength elements. Spoon- or U-shaped opx/cpx REE partitioning patterns are observed in all the abyssal peridotite samples included in this study. Four of the nine mantle xenoliths that have lower REE closure temperature also exhibit spoon-shaped REE partitioning pattern. Through simple forward modeling, we have shown that the spoon- or U-shaped opx/cpx REE partitioning patterns can be produced by disequilibrium melting followed by diffusive exchange between cpx and opx at subsolidus state. It may be possible to deduce cooling rate and thermal history through detailed modeling of REE in coexisting cpx and opx and spoon-shaped opx/cpx REE partitioning patterns in mantle samples. A prerequisite in subsolidus modeling is the initial concentrations of REE in cpx and opx at the onset of cooling which corresponds to the end of the disequilibrium melting modeling. The present study has set a stage for such endeavors in the future.

ACKNOWLEDGEMENTS

We thank Daniele Brunelli, Henry Dick, Jingao Liu, and Jessica Warren for useful discussion regarding grain size in peridotites, and Suzanne Birner for helpful comments and suggestions on an earlier version of this manuscript. This work was supported by National Science Foundation grant EAR-1852088 and the China Scholarship Council (201806010079).

APPENDIX A. GOVERNING EQUATIONS

The disequilibrium double-porosity melting model of Liang and Liu (2016) is intended for modeling trace element fractionation during concurrent melting, channelized melting extraction, and finite rate of crystal-melt chemical exchange in an upwelling steady-state melting column. In terms of the degree of melting experienced by the solid matrix (F), mass conservation equations for a trace element in the interstitial melt (C_f), residual solid (C_s), individual mineral (C_s^j) can be written as:

$$\varepsilon_{cpx}(1-\mathbb{R})F\frac{\mathrm{d}C_f}{\mathrm{d}F}=\varepsilon_{\mathrm{cpx}}\left(C_s^p-C_f\right)+\sum_{j=1}^{N}w_j\frac{R_j}{R_{cpx}}\left(C_s^j-k_jC_f\right) \quad (A1a)$$

$$\varepsilon_{cpx}\ (1-F)\frac{\mathrm{d}C_s}{\mathrm{d}F}=\varepsilon_{cpx}\left(C_s-C_s^p\right)-\sum_{j=1}^{N}w_j\frac{R_j}{R_{cpx}}\left(C_s^j-k_jC_f\right) \quad (A1b)$$

$$\varepsilon_{\mathrm{cpx}}\,(1-F)\frac{\mathrm{d}C_s^j}{\mathrm{d}F}=-\frac{R_j}{R_{cpx}}\left(C_s^j-k_jC_f\right) \quad (A1c)$$

where k_j is the partition coefficient between mineral j and melt for the element of interest; $\mathbb{R}$ is the dimensionless melt suction rate defined as the fraction of melt removed from the residual solid (to a nearby channel) relative to the amount of melt produced by melting (Iwamori, 1994; Liang and Peng, 2010); ε_{cpx} is the disequilibrium parameter for a trace element in cpx; C_s^p is the concentration of bulk solid calculated according to melting reaction; and w_j is the weight fraction of mineral j in residual solid. The latter three parameters are defined as follows:

$$\varepsilon_{\mathrm{cpx}}=\frac{\Gamma}{\rho_s(1-\phi_f)R_{cpx}} \quad (A1d)$$

$$C_s^p=\sum_{j=1}^{N}w_j^pC_s^j \quad (A1e)$$

$$\mathrm{w_j}=\frac{w_j^0-w_j^pF}{1-F} \quad (A1f)$$

where Γ is the melting rate; ρ_s is the density of the bulk solid; ϕ_f is the volume fraction of the melt in the residue; w_j^0 is the weight fraction of mineral j at the onset of the melting; and w_j^p is the weight fraction of mineral j participating in the melting reaction. Equations (A1a)-(A1c) can be further simplified by assuming that the interstitial melt and olivine and spinel are location chemical equilibrium. The mass conservation equations become:

$$\left(\varepsilon_{\mathrm{cpx}}(1-\mathbb{R})F+\varepsilon_{\mathrm{cpx}}(1-F)\left(w_{ol}k_{ol}+w_{sp}k_{sp}\right)\right)\frac{\mathrm{d}C_f}{\mathrm{d}F}=$$

$$\varepsilon_{\mathrm{cpx}}\left(C_s^p-C_f\right)+w_{cpx}\left(C_s^{cpx}-k_{cpx}C_f\right)+w_{opx}\frac{R_{opx}}{R_{cpx}}\left(C_s^{opx}-k_{opx}C_f\right) \quad \text{(A2a)}$$

$$\varepsilon_{\mathrm{cpx}}(1-F)\frac{\mathrm{d}C_s^{cpx}}{\mathrm{d}F}=-\left(C_s^{cpx}-k_{cpx}C_f\right) \quad (A2b)$$

$$\varepsilon_{\mathrm{cpx}}(1-F)\frac{\mathrm{d}C_s^{opx}}{\mathrm{d}F}=-\frac{R_{opx}}{R_{\mathrm{cpx}}}\left(C_s^{opx}-k_{opx}C_f\right) \quad (A2c)$$

$$C_s^p=\ w_{cpx}^pC_s^{cpx}+w_{opx}^pC_s^{opx}+w_{ol}^pk_{ol}C_f+w_{sp}^pk_{sp}C_f \quad (A2d)$$

Concentration of REE in the bulk residue can be calculated using the expression:

$$C_s=\sum w_jC_s^j\ =\ w_{cpx}\,C_s^{cpx}+w_{opx}\,C_s^{opx}+w_{ol}\,k_{ol}C_f+w_{sp}\,k_{sp}C_f \quad (A2e)$$

Equations (A2a)-(A2c) are closed by the following boundary conditions at the bottom of the melting column ($F = 0$):

$$C_f(0)=\frac{\varepsilon_{\mathrm{cpx}}\,k_p+k_0}{k_0\left(\varepsilon_{\mathrm{cpx}}+k_0\right)}C_s^0 \quad (A2f)$$

$$C_s^{cpx}(0)=\frac{k_{cpx}}{k_0}\,C_s^0 \quad (A2g)$$

$$C_s^{opx}(0)=\frac{k_{opx}}{k_0}C_s^0 \quad (A2h)$$

where k_0 is the bulk solid–melt partition coefficient at the onset of melting; and k_p is the bulk solid–melt partition coefficient according to the melting reaction. Equation (A2f) is based on the analysis of Liang and Liu (2016). Equations (A2a)-(A2c) are a set of coupled ordinary differential

792 equations and can be solved numerically using standard methods. In this study, we solve these
793 equations using the routine ODEIENT in Python.

794

795

References

Agranier A. and Lee C. T. A. (2007) Quantifying trace element disequilibria in mantle xenoliths and abyssal peridotites. Earth Planetary Science Letter **257**, 290–298.

Anders E. and Grevsse N. (1989) Abundances of the elements: Meteoritic and solar. Geochimica et Cosmochimica Acta **53**, 197–214.

Baker M. B. and Stolper E. M. (1994) Determining the composition of high–pressure mantle melts using diamond aggregates. Geochimica et Cosmochimica Acta **58**, 2811–2827.

Baker M. B. and Stolper E. M. (1994) Determining the composition of high-pressure mantle melts using diamond aggregates. Geochimica et Cosmochimica Acta **58**, 2811–2827.Bedini R. and Bodinier J. L. (1999) Distribution of incompatible trace elements between the constituents of spinel peridotite xenoliths: ICP–MS data from the East African Rift. Geochimica et Cosmochimica Acta **63**, 3883–3900.

Bodinier J-L. and Godard M. (2014) Orogenic, ophiolitic, and abyssal peridotites. In *Treatise on Geochemistry: The Mantle and Core* 2nd Edition (ed. R. W. Carlson). Elsevier, New York. pp. 103-167.

Bodinier J. L., Vasseur G., Vernieres J., Dupuy C. and Fabries J. (1990) Mechanisms of Mantle Metasomatism: Geochemical Evidence from the Lherz Orogenic Peridotite. Journal of Petrology **31**, 597–628.

Brey G. and Kohler T. (1990) Geothermobarometry in four–phase lherzolites II. New thermobarometers, and practical assessment of existing thermobarometers. Journal of Petrology **31**, 1353–1378.

Brunelli D. and Seyler M. (2010) Asthenospheric percolation of alkaline melts beneath the St. Paul region (Central Atlantic Ocean). Earth Planetary Science Letter 289, 393–405.

Brunelli D., Paganelli E. and Seyler M. (2014) Percolation of enriched melts during incremental open–system melting in the spinel field: a REE approach to abyssal peridotites from the Southwest Indian Ridge. Geochimica et Cosmochimica Acta **127**, 190–203.

Brunelli D., Seyler M., Cipriani A., Ottolini L. and Bonatti E. (2006) Discontinuous melt extraction and weak refertilization of mantle peridotites at the Vema Lithospheric Section (Mid– Atlantic Ridge). Journal of Petrology **47**, 745–771.

Cherniak D. J. (2015) Nb and Ta diffusion in titanite. Chemical Geology **413**, 44–50.

Cherniak D. J. and Liang Y. (2007) Rare earth element diffusion in natural enstatite. Geochimica et Cosmochimica Acta **71**, 1324–1340.

D'Errico M. E., Warren J. M. and Godard M. (2016) Evidence for chemically heterogeneous Arctic mantle beneath the Gakkel Ridge. Geochimica et Cosmochimica Acta **174**, 291–312.

Dick H. J. B. and Bullen T. (1984) Chromian spinel as a petrogenetic indicator in abyssal and alpine–type peridotites and spatially associated lavas. Contributions to Mineralogy and Petrology **86**, 54–76.

Dygert N. and Liang Y. (2015) Temperatures and cooling rates recorded in REE in coex– isting pyroxenes in ophiolitic and abyssal peridotites. Earth Planetary Science Letter **420**, 151–161.

Dygert N., Kelemen P. B. and Liang, Y. (2017) Spatial variations in cooling rate in the mantle section of the Samail ophiolite in Oman: Implications for formation of lithosphere at mid–ocean ridges. Earth and Planetary Science Letters **465**, 134–144.

Ghiorso M. S., Hirschmann M. M., Reiners P. W. and Kress V. C. (2002) The pMELTS: a revision of MELTS for improved calculation of phase relations and major element partitioning related to partial melting of the mantle to 3 GPa. Geochemistry, Geophysics, Geosystems **3**, 1–35.

Harvey J., Yoshikawa M., Hammond S. J. and Burton K. W. (2012) Deciphering the trace element characteristics in Kil–bourne Hole peridotite xenoliths: melt–rock interaction andmetasomatism beneath the Rio Grande Rift, SW USA. Journal of Petrology **53**, 1709–1742.

Hellebrand E. and Snow J. E. (2003) Deep melting and sodic metasomatism underneath the highly oblique–spreading Lena Trough (Arctic Ocean). Earth and Planetary Science Letters **216**, 283–299.

Hellebrand E., Snow J. E., Dick H. J. B. and Hofmann A. W. (2001) Coupled major and trace elements as indicators of theextent of melting in mid–ocean–ridge peridotites. Nature **410**,677–681.

Hellebrand E., Snow J. E., Hoppe P. and Hofmann A. W. (2002) Garnet–field melting and late–stage refertilization in 'residual' abyssal peridotites from the Central Indian Ridge. Journal of Petrology **43**, 2305–2338.

Hellebrand E., Snow J. E., Mostefaoui S. and Hoppe P. (2005) Trace element distribution between orthopyroxene and clinopyroxene in peridotites from the Gakkel Ridge: a SIMS and NanoSIMS study. Contributions to Mineralogy and Petrology **150**, 486–504.

Iwamori H. (1994) ^{238}U–^{230}Th–^{226}Ra and ^{235}U–^{231}Pa disequilibria produced by mantle melting with porous and channel flows. Earth and Planetary Science Letters **125**, 1–16.

Johnson K. T. M. (1998) Experimental determination of partition coefficients for rare earth and high–field–strength elements between clinopyroxene, garnet, and basaltic melt at high pressures. Contributions to Mineralogy and Petrology **133**, 60–68.

Johnson K. T. M. and Dick H. J. B. (1992) Open system melting and temporal and spatial variation of peridotite and basalt at the Atlantis II Fracture Zone. Journal of Geophysical Research: Solid Earth 97, 9219–9241.

Johnson K. T. M., Dick H. J. B. and Shimizu N. (1990) Melting in the oceanic upper mantle: an ion microprobe study of diopsides in abyssal peridotites. Journal of Geophysical Research: Solid Earth **95**, 2661–2678.

Jull M., Kelemen P. B., Sims K. (2002) Consequences of diffuse and channelled porous melt migration on uranium series disequilibria. Geochimica et Cosmochimica Acta 66, 4133-4148.

Kelemen P. B., Hirth G., Shimizu N., Spiegelman M. and Dick H. J. B. (1997) A review of melt migration processes in the adiabatically upwelling mantle beneath oceanic spreading ridges. Philosophical Transactions: Mathematical, Physical and Engineering Science **355**, 283–318.

Key K., Constable S., Liu L., and Pommier A. (2013) Electrical image of passive mantle upwelling beneath the northern East Pacific Rise. Nature 495, 499-502.

Kinzler R. J. and Grove T. L. (1992) Primary magmas of mid-ocean ridge basalts 1. Experiments and methods. Journal of Geophysical Research: Solid Earth **97**, 6885–6906.

Lee C. T. A., Harbert A. and Leeman W. P. (2007) Extension of lattice strain theory to mineral/mineral rare–earth element partitioning: An approach for assessing disequilibrium and developing internally consistent partition coefficients between olivine, orthopyroxene, clinopyroxene and basaltic melt. Geochimica et Cosmochimica Acta **71**, 481–496.

Liang Y. (2003) On the thermo–kinetic consequences of slab melting. Geophysical Research Letter **30**, 2270. http://dx.doi.org/ 10.1029/2003GL018969.

Liang Y. (2014) Time scales of diffusive re–equilibration in bi–mineralic systems with and without a fluid or melt phase. Geochimica et Cosmochimica Acta **132**, 274–287.

Liang Y. and Liu B. (2016) Simple models for disequilibrium fractional melting and batch melting with application to REE fractionation in abyssal peridotites. Geochimica et Cosmochimica Acta **173**, 181–197.

Liang Y. and Peng Q. (2010) Non–modal melting in an upwelling mantle column: steady–state models with applications to REE depletion in abyssal peridotites and the dynamics of melt migration in the mantle. Geochimica et Cosmochimica Acta **74**, 321– 339.

Liang Y., Sun C. and Yao L. (2013) A REE–in–two–pyroxene thermometer for mafic and ultramafic rocks. Geochimica et Cosmochimica Acta **102**, 246–260.

Liu B. and Liang Y. (2017) An introduction of Markov chain Monte Carlo method to geochemical inverse problems: Reading melting parameters from REE bundances in abyssal peridotites. Geochimica et Cosmochimica Acta **203**, 216–234.

Liu B. and Liang Y. (2019) Importance of permeability and deep channel network on the distribution of melt, fractionation of REE in abyssal peridotites, and U-series

disequilibria in basalts beneath mid-ocean ridges: A numerical study using a 2D double-porosity model. Earth Planetary Science Letters 528, 115788.

Liu C.–Z., Snow J. E., Hellebrand E., Brugmann G., von der Handt A., Buchl A. and Hofmann A. W. (2008) Ancient, highly heterogeneous mantle beneath Gakkel ridge, Arctic Ocean. Nature **452**, 311–316.

Liu J., Carlson R. W., Rudnick R. L., Walker R. J., Gao S. and Wu F. (2012) Comparative Sr–Nd–Hf–Os–Pb isotope systematics of xenolithic peridotites from Yangyuan, North China Craton: additional evidence for a Paleoproterozoic age. Chemical Geology **332**, 1–14.

Lundstrom C. (2000) Models of U–series disequilibria generation in MORB: the effects of two scales of melt porosity. Physics of the Earth and Planetary Interiors **121**, 189–204.

McDonough W. F. and Sun S. S. (1995) The composition of the Earth. Chemical Geology **120**, 223–253.

Navon O. and Stolper E. (1987) Geochemical consequences of melt percolation: the upper mantle as a chromatographic column. The Journal of Geology **95**, 285–307.

Niu Y. and He´kinian R. (1997) Spreading–rate dependence of the extent of mantle melting beneath ocean ridges. Nature 385, 326– 329.

Quinn D. P., Saleeby J., Ducea M., Luffi P. and Asimow P. (2018) Late–Cretaceous con–struction of the mantle lithosphere beneath the central California coast revealed by Crystal Knob xenoliths. Geochemistry, Geophysics, Geosystems **19**, 3302–3346.

Salters V. J. M. and Dick H. J. B. (2002) Mineralogy of the mid– ocean–ridge basalt source from neodymium isotopic composition of abyssal peridotites. Nature **418**, 68–72.

Sambridge M. and Mosegaard K. (2002) Monte Carlo methods in geophysical inverse problems. Reviews of Geophysics **40**, 1009.

Sanfilippo A., Salters V., Tribuzio R. and Zanetti A. (2019) Role of ancient, ultra–depleted mantle in mid–ocean–ridge magmatism. Earth Planetary Science Letter **511**, 89–98.

Seyler M., Brunelli D., Toplis M. J. and Me´vel C. (2011) Multiscale chemical heterogeneities beneath the eastern Southwest Indian Ridge (52° E–68° E): Trace element compositions of along–axis dredged peridotites. Geochemistry, Geophysics, Geosystems 12, Q0AC15, doi:10.1029/2011GC003585.

Shimizu N. (1998) The geochemistry of olivine–hosted melt inclusions in a FAMOUS basalt ALV519–4–1. Physics of the Earth and Planetary Interiors **107**, 183–201.

Stosch H. G. (1982) Rare earth element partitioning between minerals from anhydrous spinel peridotite xenoliths. Geochimica et Cosmochimica Acta **46**, 793–811.

Stracke A., Genske F., Berndt J. and Koornneef J. M. (2019) Ubiquitous ultra–depleted domains in Earth's mantle. Nature Geoscience **12**, 851–855.

939 Stracke A., Snow J. E., Hellebrand E., von der Handt A., Bourdon B., Birbaum K. and Günther,
940 D. (2011) Abyssal peridotite Hf isotopes identify extreme mantle depletion. Earth
941 Planetary Science Letter **308**, 359–368.

942 Sun C. and Liang, Y. (2014) An assessment of subsolidus re–equilibration on REE distribution
943 among mantle minerals olivine, orthopyroxene, clinopyroxene, and garnet in peridotites.
944 Chemical Geology **372**, 80–91.

945 Van Orman J. A., Grove T. L. and Shimizu N. (2001) Rare earth element diffusion in diopside;
946 influence of temperature, pressure, and ionic radius, and an elastic model for diffusion in
947 silicates. Contributions to Mineralogy and Petrology **141**, 687–703.

948 Van Orman J. A., Grove T. L. and Shimizu N. (2002) Diffusive fractionation of trace elements
949 during production and transport of melt in Earth's upper mantle. Earth Planetary Science
950 Letter **198**, 93–112.

951 Voigt M. and von der Handt A. (2011) Influence of subsolidus processes on the chromium
952 number in spinel in ultramafic rocks. Contributions to Mineralogy and Petrology **162**,
953 675–689.

954 Walter M. J. and Presnall D. C. (1994) Melting behavior of simplified lherzolite in the system
955 $CaO–MgO–Al_2O_3–SiO_2–Na_2O$ from 7 to 35 kbar. Journal of Petrology **35**, 329–359.

956 Wang C., Liang Y. and Xu W. (2015) On the significance oftemperatures derived frommajor
957 element and REE based two–pyroxene thermometers for mantle xenoliths from the North
958 China Craton. Lithos **224–225**, 101–113.

959 Warren J. M. (2016) Global variations in abyssal peridotite compositions. Lithos **248–251**,193–
960 219.

961 Warren J. M., Shimizu N., Sakaguchi C., Dick H. J. B. and Nakamura E. (2009) An assessment
962 of upper mantle heterogeneity based on abyssal peridotite isotopic compositions. Journal
963 of Geophysical Research 114, B122023, doi:10.1029/2008JB006186.

964 Witt–Eickschen G. and O'Neill H. S. C. (2005) The effect of temperature on the equilibrium
965 distribution of trace elements between clinopyroxene, orthopyroxene, olivine and spinel
966 in upper mantle peridotite. Chemical Geology **221**, 65–101.

967 Workman R. K. and Hart S. R. (2005) Major and trace element composition of the depleted
968 MORB mantle (DMM). Earth Planetary Science Letter **231**, 53–72.

969 Yang Y. Forsyth D. W., and Weeraratne D. S. (2007) Seismic attenuation near the East Pacific
970 Rise and the origin of the low-velocity zone. Earth Planet. Sci. Lett. 258, 260-268.

971 Yao L. (2015) Closure Temperature and Closure Pressure in Bi–Mineralic Systems with
972 Applications to REE–in–Two–Mineral Thermobarometers. Brown University Ph.D.
973 thesis.

974 Yao L. and Liang Y. (2015) Closure temperature in cooling bi–mineralic systems: I. Definition
975 and with application to REE–in–two–pyroxene thermometer. Geochimica et
976 Cosmochimica Acta **162**, 137–150.

977

Figures

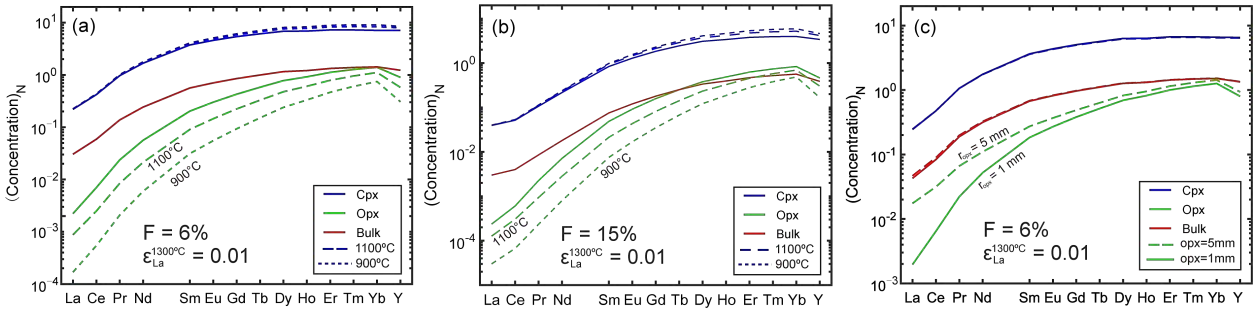

Fig. 1. (a) Forward simulation of REE patterns in residual solid, clinopyroxene (cpx), and orthopyroxene (opx) after 6% disequilibrium melting followed by subsolidus reequilibration. The solid lines represent REE patterns calculated using the disequilibrium melting model and melting parameters of $\varepsilon_{La}^{1300} = 0.01$ and $\mathbb{R} = 0.95$. The dashed lines represent the recalculated REE concentrations in the two pyroxenes at 1100ºC and 900ºC. (b) same as (a) but with 15% melting. (c) Comparison of REE patterns in residual solid, cpx, and opx after 6% disequilibrium melting for two choices of opx grain size. The solid lines represent the case of r_{cpx} = 1 mm and the dashed lines are for r_{opx} = 5 mm. The grain size of cpx is assumed to be 1 mm. Parameters used in this simulation are as same as in (a). The temperature-dependent cpx-opx partition coefficients are from Sun and Liang (2014). Concentrations of REE are normalized to CI chondrite using the values of Anders and Grevesse (1989).

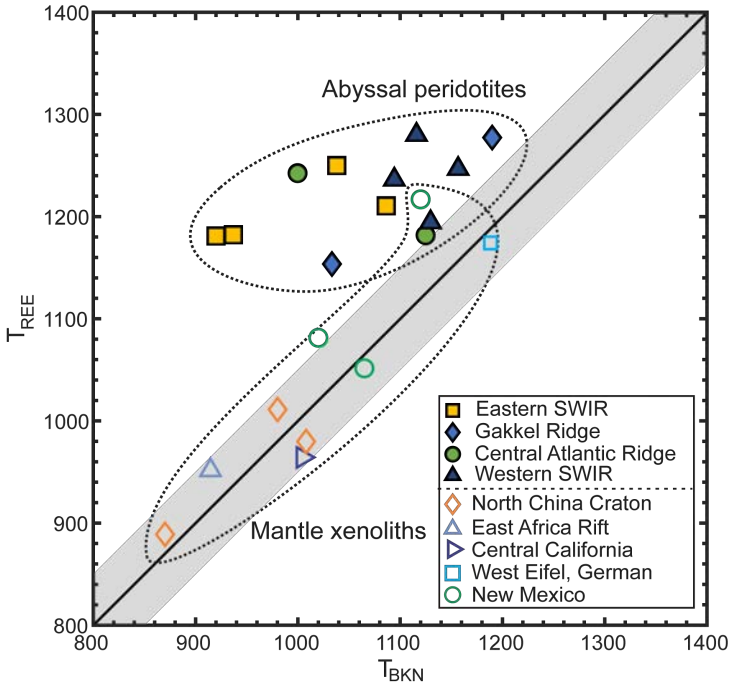

995

996 Fig. 2. Comparison of the temperatures derived from the REE-in-two-pyroxene thermometer of
997 Liang et al. (2013, T_{REE}) and those calculated using the two-pyroxene thermometer of Brey and
998 Kohler (1990, T_{BKN}) for the 9 mantle xenoliths and 12 abyssal peridotites included in this study
999 (see text for a list of the source of data). All calculations were performed assuming a pressure of
1000 1.5 GPa.

1001

1002

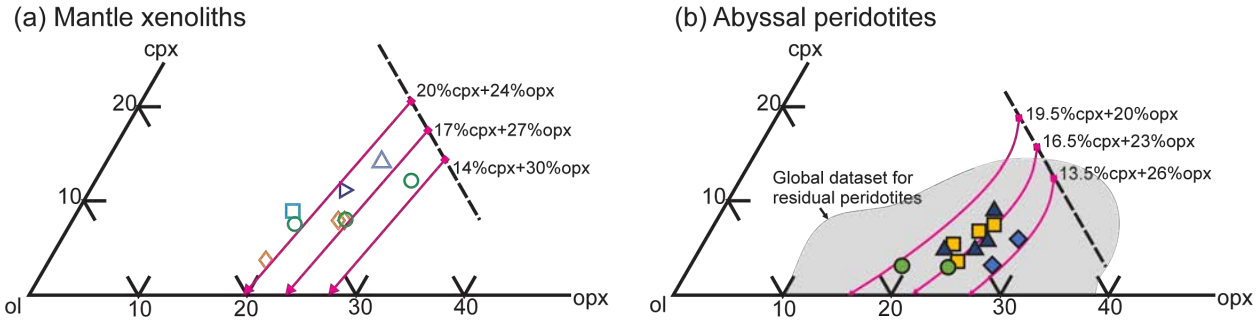

1003

1004 Fig. 3. Modal abundances of clinopyroxene (cpx), orthopyroxene (opx), and olivine (ol) in mantle
1005 xenoliths (a) and abyssal peridotites (b) selected in this study. The magenta lines in (a) are
1006 calculated using the melting reaction of Baker and Stolper (1994): 0.38 opx + 0.71 cpx + 0.13
1007 spinel = 0.22 olivine +1 melt and for three choices of starting mantle mode. The light grey area in
1008 (b) is based on Warren (2016) for residual abyssal peridotites from around the world. The magenta
1009 curves in (b) represent melting paths based on pMELTS with potential temperature of 1330 °C and
1010 150 ppm water content and three choices of starting mantle mode. Sample legends are the same as
1011 in Fig. 2.

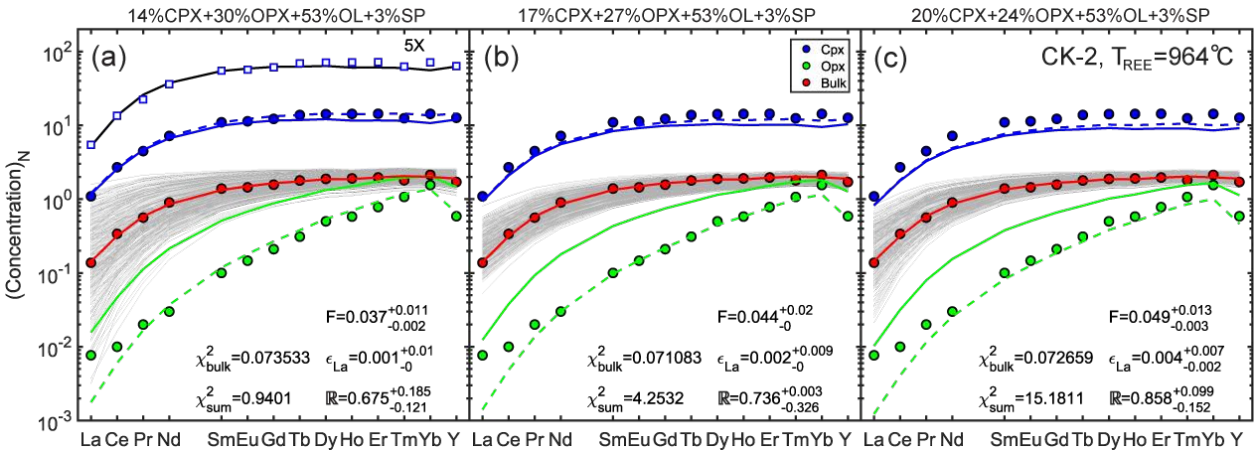

Fig. 4. Comparison between observed (circles) and model derived (curves) REE+Y patterns in the bulk and two pyroxenes in the xenolith sample CK-2 (Quinn et al., 2018). Simulation results for three starting mantle modes are shown in panels (a), (b), and (c). The grey solid curves are MCMC predictions and the red solid curve represents the best-fit of the bulk REE+Y data. The solid blue and green curves represent the calculated REE abundances in cpx and opx, respectively, based on the inversed melting parameters of the best-fit of the bulk data. The dashed blue and green curves represent the model predicted subsolidus REE abundances in cpx and opx at $T = T_{REE}$, calculated using the temperature-dependent cpx-opx partition coefficients of Sun and Liang (2014). The sum of Pearson's Chi-square (χ^2_{sum}) is the sum of the Chi-squares of simulated bulk (red curve) and simulated cpx and opx after subsolidus re-equilibrium (dashed bulk and green curves). The open squares and black curve in (a) represent the cpx data and the best-fit result based on the cpx-alone melting model. For clarity, data from cpx-alone simulations were elevated by a factor of 5. Concentrations of REE are normalized to CI chondrite using the values of Anders and Grevesse (1989).

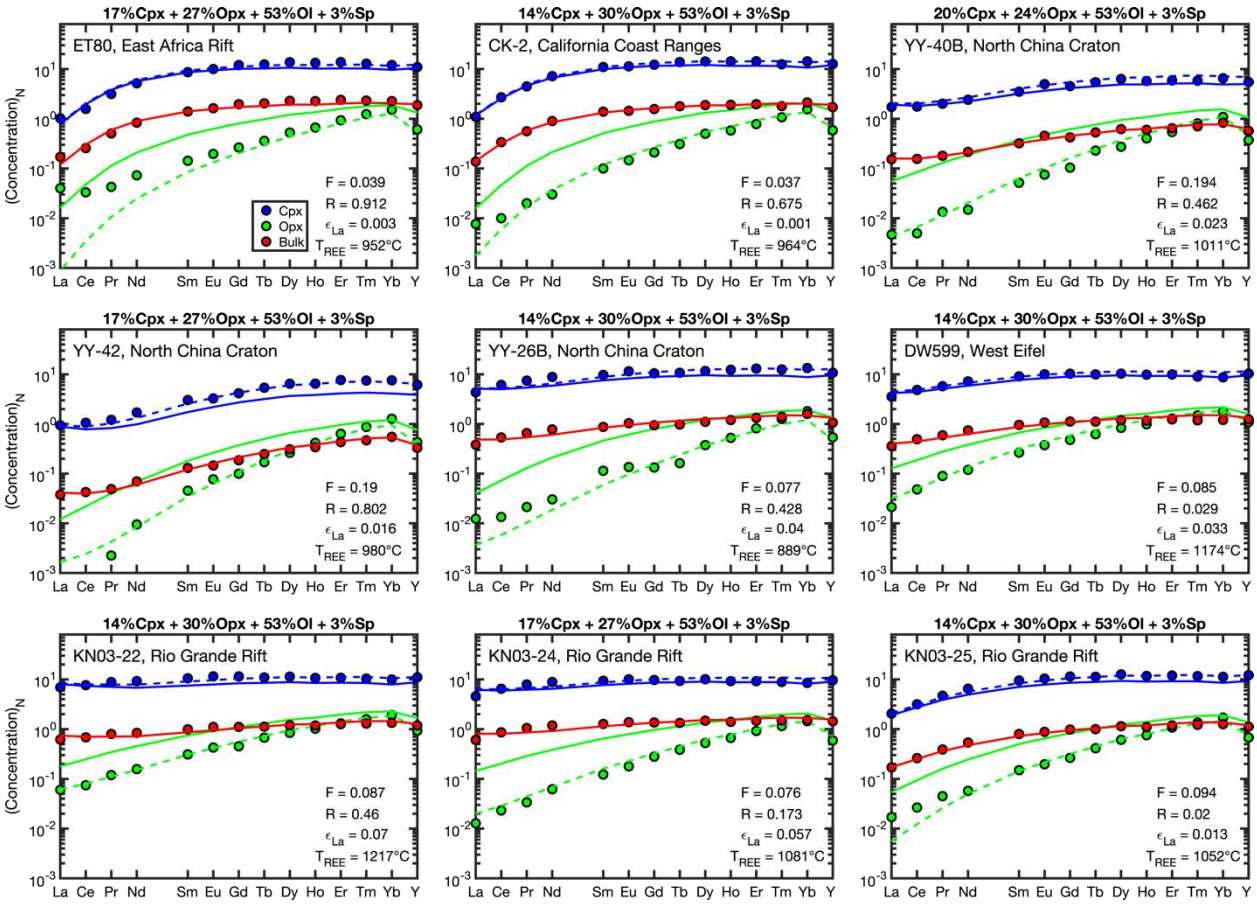

Fig. 5. Summary of preferred models for the nine mantle xenolith samples with REE + Y in the primitive mantle as starting mantle compositions. Modal abundance of the starting mantle is listed for each sample. The solid red curves are the best-fits of the bulk REE + Y data (circles). The solid blue and green curves represent the calculated REE concentrations in cpx and opx, respectively, based on the inversed melting parameters. The dashed blue and green curves represent the model predicted subsolidus REE abundances in cpx and opx at $T = T_{REE}$, calculated using the temperature-dependent cpx-opx partition coefficients of Sun and Liang (2014). Results of MCMC simulations with PM and DMM starting compositions for the nine xenolith samples are presented in supplementary Fig. S4 and Tables S1b and S2.

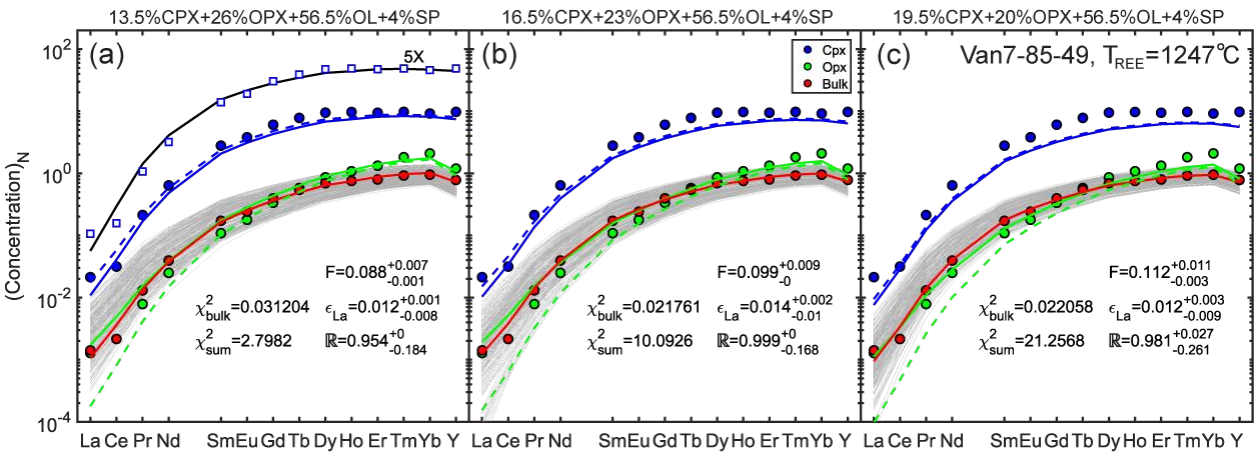

Fig. 6. Comparison between observed (circles) and model derived (curves) REE+Y patterns in the bulk and two pyroxenes in the abyssal peridotite sample Van7-85-49 (Warren et al., 2009). For a detailed explanation of symbols and curves, a reader is referred to the caption to Fig. 4.

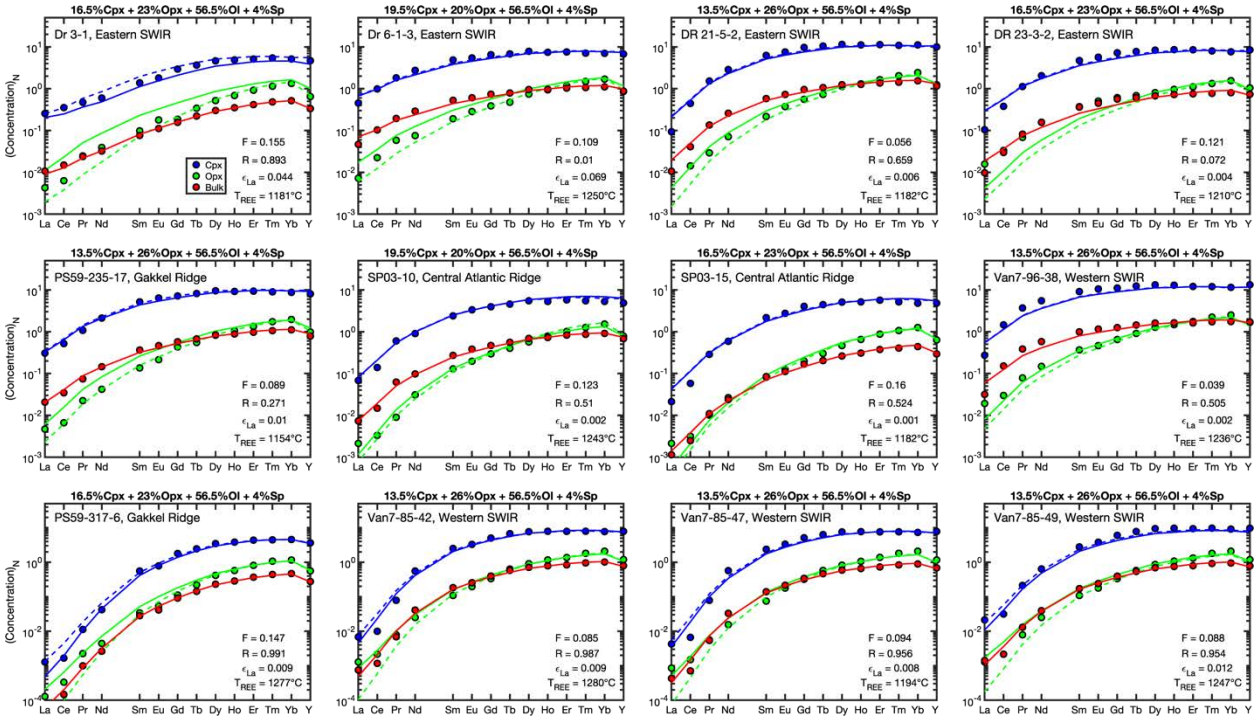

Fig. 7. Summary of preferred models for the twelve abyssal peridotite samples with REE + Y in DMM as starting mantle compositions. Modal abundance of the starting mantle is listed for each sample. Supplementary Fig. S5 presents detailed simulation results for individual samples. Supplementary Tables S1c and S2 provide additional information on uncertainties of preferred melting parameters, Pearson's Chi-squares, and results from cpx alone inversion. Symbols are the same as those described in the caption to Fig. 5.

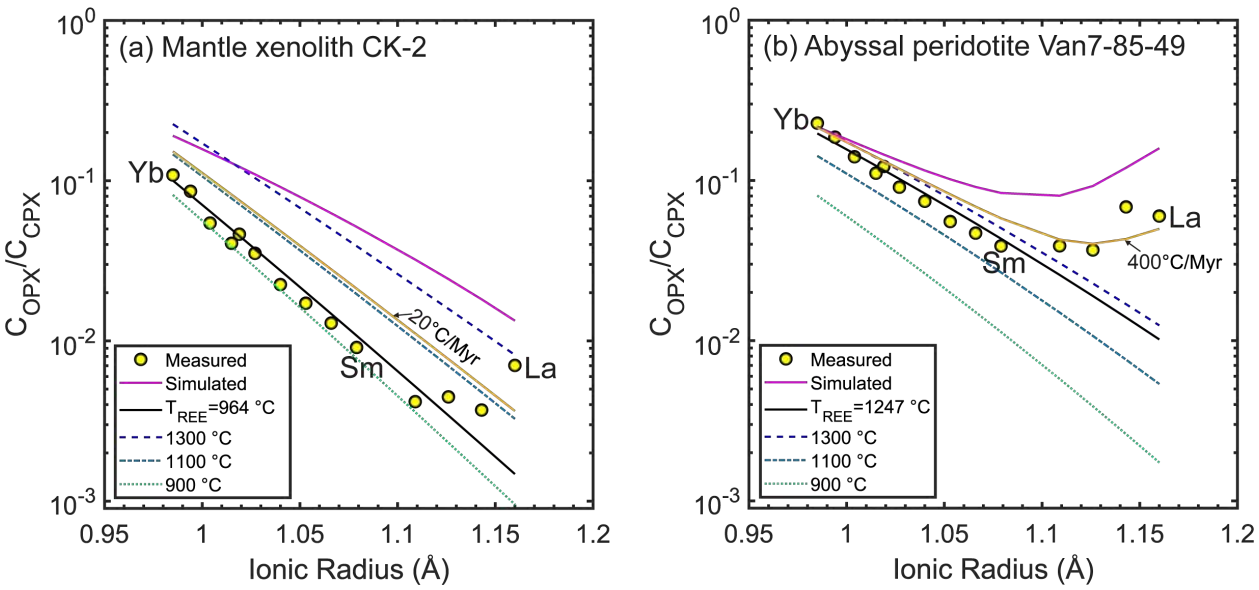

Fig. 8. Variations of the apparent opx-cpx REE partition coefficient as a function of REE ionic radius for the xenolith sample CK-2 (a) and abyssal peridotite Van7-85-49 (b). The yellow circles represent the measured data. The magenta and black curves represent the model predicted apparent partition coefficients at the end of melting and at the subsoliduis temperature $T = T_{REE}$, respectively. The thin orange curves were calculated using a simple model for diffusive reequilibration between two minerals at the stated cooling rates. The three dashed curves are the calculated opx-cpx REE partition coefficients using the model of Sun and Liang (2014).

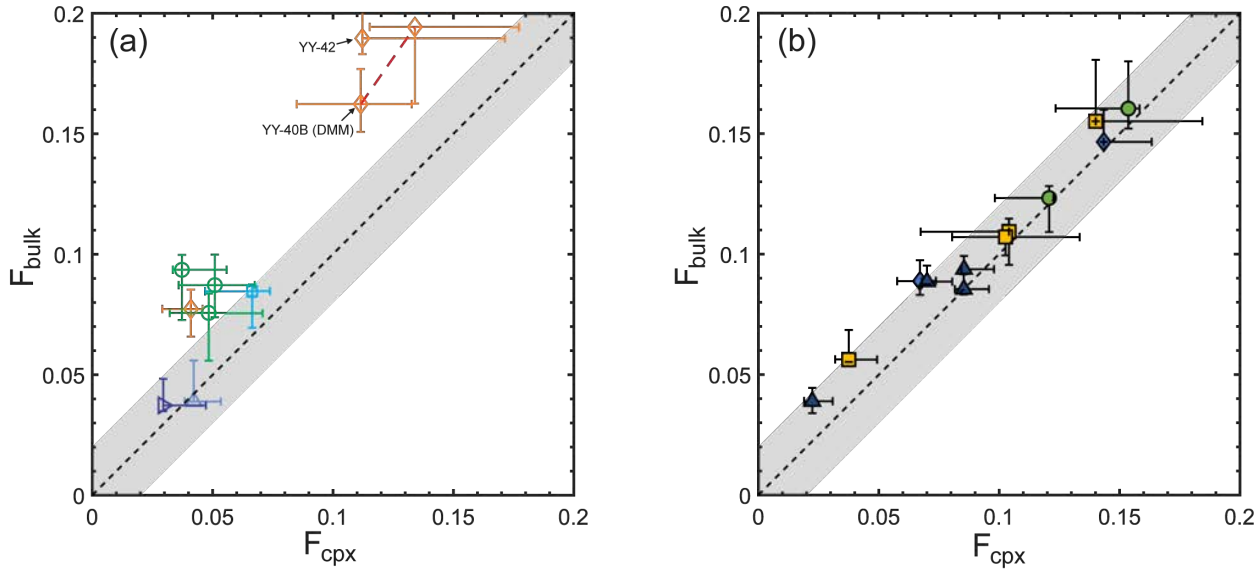

Fig. 9. Comparison of the degree of melting derived from the cpx-alone inversion (F_{cpx}) and the degree of melting derived from inversion of the bulk sample (F_{bulk}) for the mantle xenoliths (a) and abyssal peridotites (b) selected in this study. The dashed lines and grey areas represent the 1:1 ratio within a ±2% range. The red dashed line in (a) connects the inversion results of sample YY-

40B with primitive mantle (PM) and the depleted MORB mantle (DMM) starting compositions. Error bars are based on MCMC simulations. Sample legends are the same as in Fig. 2.

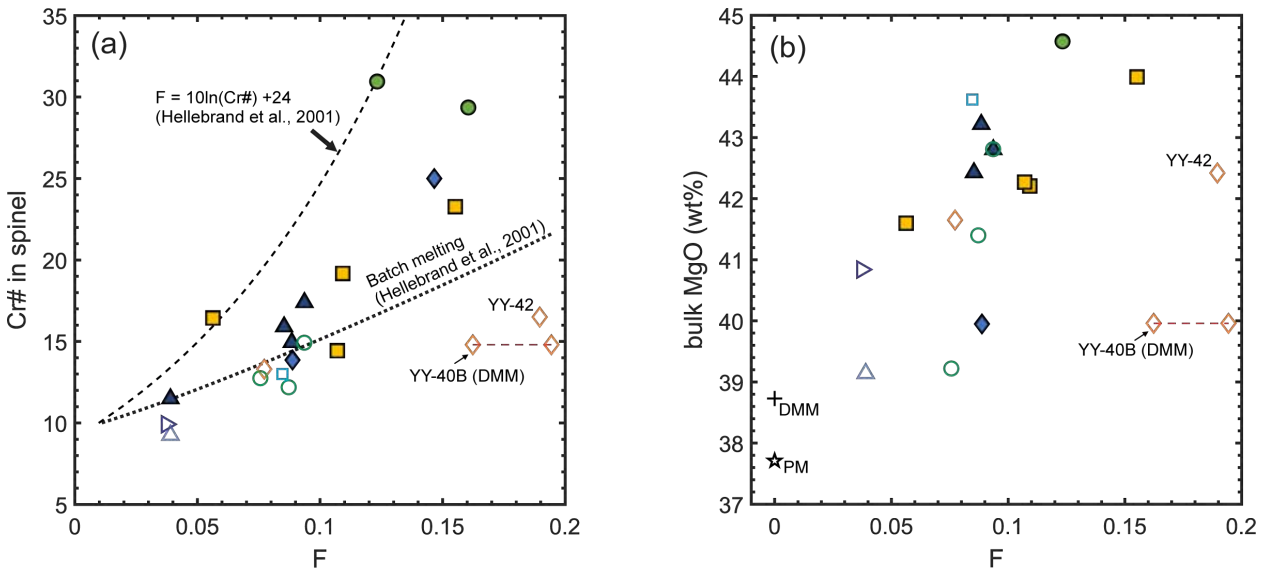

Fig. 10. Variations of spinel Cr# (a) and bulk MgO content (b) as a function of the degree of melting for the mantle xenoliths (open symbols) and abyssal peridotites (filled symbols) included in this study. The two dashed lines are based on the empirical expressions of Hellebrand et al. (2001) for fractional and batch melting. Symbols are the same as in Fig. 2.